Thermal evolution of Permian post-orogenic extension and Jurassic rifting recorded in the Austroalpine basement (SE Switzerland, N Italy)

Benoit Petri, Ja Wijbrans, Geoffroy Mohn, Gianreto Manatschal, Marco Beltrando

THERMAL EVOLUTION OF PERMIAN POST-OROGENIC EXTENSION AND JURASSIC RIFTING RECORDED IN THE AUSTROALPINE BASEMENT (SE SWITZERLAND, N ITALY)

B. Petri[1], J.R. Wijbrans[2], G. Mohn[3], G. Manatschal[1], M. Beltrando[4,*]

[1] Institut Terre et Environnement de Strasbourg, Université de Strasbourg, CNRS, UMR7063, F-67084 Strasbourg, France

[2] Department of Earth Sciences, Vrije Universiteit Amsterdam, 1081 HV Amsterdam, The Netherlands

[3] Département Géosciences et Environnement, CY Cergy Paris Université, 95000 Cergy-Pontoise, France

[4] Departimento di Scienze della Terra, Università di Torino, 10125 Torino, Italy

[*] Deceased 8th December 2015

Author contact: bpetri@unistra.fr

Short title: Middle crust cooling history

Citation: Petri, B., Wijbrans, J.R., Mohn, G., Manatschal, G., Beltrando, M., 2023. Thermal evolution of Permian post-orogenic extension and Jurassic rifting recorded in the Austroalpine basement (SE Switzerland, N Italy). Lithos 107124. https://doi.org/10.1016/j.lithos.2023.107124

HIGHLIGHTS

- New Ar-ages are reported from the Alpine Tethys necking zone.
- A slow (5-10 °C/Myr) post-Variscan cooling is identified in the Grosina unit.
- A rapid (25-100 °C/Myr) Jurassic cooling is identified in the necking zone.
- A re-heating is suspected during the necking of the Alpine Tethys rifted margin.
- The thermal evolution is constrained by Monte Carlo simulations based on DiffArgP.

ABSTRACT

The thermal evolution of the continental lithosphere is intimately linked to its tectonic history. In the present contribution, we explore the thermal evolution of the Austroalpine Campo and Grosina units that composed the former necking zone of the Adriatic rifted margin and that are now exposed in the Eastern Alps (SE Switzerland and N Italy). The Campo unit and the overlying Grosina unit are separated by a Jurassic horizontal extensional structure, the Eita shear zone. We report new muscovite and biotite $^{40}Ar/^{39}Ar$ ages for the Grosina unit (~261 Ma for muscovite and ~246-245 Ma for biotite) and for the Campo unit (~218-178 Ma for muscovite and ~214-171 Ma for biotite). No geologically meaningful amphibole ages were obtained because of contamination by extraneous argon in these minerals. The new results are combined with published ages obtained with different chronometers (U–Pb, Sm–Nd, Rb–Sr, K–Ar, $^{40}Ar/^{39}Ar$). This dataset reveals that the two units record different thermal evolutions from the Permian post-orogenic extension to the Jurassic rifting. Ages of cooling initiation and associated cooling rates are estimated by Monte Carlo simulations based on DiffArgP. The Grosina unit records a Permo-Triassic slow cooling of 5-10 °C/Myr initiated during Early Permian in relation to the post-Variscan relaxation of the isotherms and cooling of the lithosphere that caused a large-scale thermal subsidence. By contrast, the Campo unit records a fast cooling of 25-100 °C/Myr associated to the tectonic exhumation of basement rocks during the Jurassic rifting and the formation of the Alpine Tethys rifted margin. This fast cooling appears delayed from major basement deformation phases, and likely follows a period of crustal re-heating.

Keywords: Post-Variscan; Alpine Tethys; Rifting; Necking zone; Austroalpine; $^{40}Ar/^{39}Ar$ ages.

1. INTRODUCTION

The interplay between tectonics, thermal evolution and topography is well exemplified by two events in an extensional cycle: the late orogenic phase (transition from an orogenic thick crust to an equilibrated ~35 km thick continental crust), and a rift event (thinning of a ~35 km thick crust to form a rifted margin and ultimately an oceanic domain).

The last stages of most orogens are characterized by the thinning of the continental crust. The reasons for the reduction in crustal thickness is still a matter of debate for some cases, with competing scenarios that include (see Rey et al., 2001 for a review): detachment or convective removal of the crustal and/or lithospheric root, slab break-off, change in far-field stress conditions or crustal strength. However, all scenarios are accompanied by a transient rise of the asthenosphere that can cause a rapid uplift together with magmatism and prograde metamorphism. As the lithosphere-asthenosphere boundary returns to thermal equilibrium, the continental crust gently subsides (e.g., Platt and England, 1994). This is the case for the Variscan orogeny in W Europe. It is characterized by the decrease in topography together with a thinning of the continental crust to reach a normal thickness of 35 ± 5 km before 310-300 Ma (Burg et al., 1994) that is immediately followed (but with a cogenetic link that remains debated) by a period of intense magmatic activity together with regional high temperature prograde metamorphism (Fig. 1a; Schuster and Stüwe, 2008). Extensional deformation is attested by both the presence of detachment faults at the surface (Pohl et al., 2018) and by several deformation structures in the basement, mostly associated to the emplacement of massive volumes of mantle-derived melts during the Early Permian (e.g., Petri et al., 2018). However, exhumation of deep crust should have been limited, as most of Permian lower crustal rocks recorded a post-HT isobaric cooling (e.g., Müntener et al., 2000; Petri et al., 2016). This is followed by a period of (relative) tectonic quiescence, characterized by a conductive cooling of the lithosphere and the associated thermal subsidence (Fig. 1ab; e.g., Prijac et al., 2000). The

detailed thermal evolution of this phase remains to be calibrated, notably the rate at which the continental crust is thermally re-equilibrated from the Permian to the Triassic.

During the formation of rifts and rifted margins, rocks are vertically displaced across the lithosphere by tectonics, but part of the topography (or the bathymetry) remains controlled by the transient thermal architecture of the crust and the lithosphere. This subsidence can be linked to the rifting history in the pure shear rift model of McKenzie (1978). However, the depth-uniform thinning implied by pure shear deformation results in lithospheric cooling only, and the more complex thermal and uplift/subsidence evolution of rifted margins can only be explained by the alternative models that integrate depth-dependant thinning. Several rift systems worldwide are indeed characterized by transient subaerial exposure and erosion (Fig. 1c; Esedo et al., 2012), followed by a rapid subsidence as soon as the thermal support lowers (Fig. 1c; e.g., Chenin et al., 2019). In remnants of the Alpine Tethys rifted margins, such an evolution is recorded in several settings. The Briançonnais domain delimited by the Valais and the Piemont-Liguria basins, is characterized by a phase of emersion attested by the presence of karst followed by a rapid subsidence during an early post-rift stage (Lemoine et al., 1986; and Mohn et al., 2011 for a review). A phase of uplift and potential basement exposure has been identified in zones of crustal necking located between (future) proximal and distal domains (Fig. 1c) by the occurrence of major unconformities and of siliciclastic sedimentary deposits sourced from the necking domain that are synchronous to major crustal thinning (i.e., crustal necking). So far 3 zones have been recognized in the Alps: the Mont Blanc massif (Ribes et al., 2020), the Gozzano-Invorio-Arona area in the Southern Alps (Decarlis et al., 2017), and suspected for the Campo and Grosina units in the Eastern Alps (Mohn et al., 2012). At depth, several lines of evidence seem to indicate that distal and necking domains are thermally supported by a short lived syn-rift phase of heating that stopped during late rifting (documented in the Southern Alps; Ewing et al., 2015; Smye and Stöckli, 2014), but details of this event (amplitude, duration) and notably its lateral extent remain unclear.

Constraining the thermal history of reactivated rifted margins remains, however, strongly hampered by the accessibility to deep crustal levels that escaped subsequent thermal overprint during the Alpine orogeny (Mohn et al., 2022). In the western end of the Eastern Alps, this can be achieved only by $^{40}Ar/^{39}Ar$ thermochronometers having closure temperatures above 300 °C, higher than the maximum temperature reached during the Alpine orogeny. Their use in pre-Alpine basement units are however complexified by a polyphase history with multiple deformation events and heating/cooling cycles. Early works identified groups of basement cooling ages related to both the Variscan (~ 390 to 290 Ma) and the Alpine (~ 60 to 20 Ma) orogenic cycles (e.g., Hunziker et al., 1992), i.e., essentially to compressive tectonic deformation phases, and authors referred to ages lying between these two bonds as “intermediate” or “mixed” ages. In recent years, several groups of ages have been proven to record extensional tectonic events too: (1) the Permian post-orogenic evolution that is characterized by widespread magmatism and prograde metamorphism associated with crustal and lithospheric extension notably documented in the Alpine realm (Manzotti et al., 2018, 2012; Petri et al., 2017; Schuster and Stüwe, 2008; Wyatt et al., 2022), and (2) the Jurassic rifting and opening of the Alpine Tethys, which resulted in the exhumation of middle to lower crustal levels (Mohn et al., 2012) with a thermal evolution that remains to be constrained. For both contexts, several key questions remain open, that can be answered by analysing the thermal evolution of the involved basement units.

The aim of the present contribution is to characterize the nature and the temperature-time evolution of the basement of the Adriatic necking zone from the Paleozoic Variscan to the Permian post-Variscan extension to the Jurassic rifting. More precisely, the goal is twofold: (1) tracking a possible post-Variscan (Permian) exhumation and/or cooling (Fig. 1ab), and (2) characterizing the exhumation of the middle-crust during rifting and its related thermal evolution (Fig. 1c). To do so, we compile structural and petrological data for both the Grosina and Campo units (Eastern Alps, N Italy and SE Switzerland) that were part of the former Adriatic necking zone and constrain their

temporal and thermal evolution with $^{40}Ar/^{39}Ar$ dating. These new ages are compared to published ages and the temperature-time evolution is constrained through Monte Carlo random simulations based on DiffArgP (Warren et al., 2012a; Wheeler, 1996).

2. TECTONIC, GEOCHRONOLOGICAL AND GEOLOGICAL FRAMEWORK

2.1. The evolution of the Austroalpine units

We focus on the Austroalpine nappes exposed along the western end of the Eastern Alps (Fig. 2a). Before being encompassed in the Alpine orogen, these nappes underwent a polyphase pre-Alpine history including the Variscan and post-Variscan evolution, and the rifting and opening of the Alpine Tethys.

2.1.1. Variscan and post-Variscan evolution

Evidence for Variscan high-pressure (HP) metamorphism and deformation are mostly reported in the western Austroalpine nappes, where crustal units reached peak metamorphic conditions during the Carboniferous. In the study area, pre-Alpine amphibolite-facies metamorphism is documented by several authors (e.g., Petri et al., 2016), and is presumed to be Variscan in age, although undated. However, evidence for Variscan-related magmatism is reported in the Bernina unit with Carboniferous plutonism of a calc-alkaline affinity (Spillmann and Büchi, 1993; von Quadt et al., 1994) with associated volcanics.

During the Permian post-Variscan event, the continental crust was affected by a prominent magmatic and metamorphic episode that deeply modified its lithological composition and crustal architecture.

(1) In the Permian upper crust, alkaline felsic magmas were emplaced and extruded between 295 and 288 Ma (Bernina unit; Spillmann and Büchi, 1993; von Quadt et al., 1994). The relation between volcanics and tectonic structures remains unclear.

(2) In the same age range, the Permian middle crust (Campo and Grosina units) was intruded by both granitoids and mafic bodies (Fig. 2b), notably the Sondalo gabbroic complex (Petri et

al., 2018, 2017; Tribuzio et al., 1999). Locally, mafic intrusions are surrounded by a migmatitic contact aureole reaching granulite-facies conditions in metasedimentary septa (Braga et al., 2001; Petri et al., 2016).

(3) The Permian lower crust was affected during the Permian by magmatic underplating through the emplacement of tholeiitic gabbros associated with felsic granulites (Malenco and Lower Margna units; Hermann et al., 2001; Müntener et al., 2000), indicating an emplacement and contact metamorphism at around 10 kbar at 281-278 Ma (U-Pb on zircon; Hansmann et al., 2001).

2.1.2. Jurassic rifting history

The post-orogenic and pre-rift Permian lithospheric architecture was disrupted during the Jurassic by a rifting event that led to the opening of the Alpine Tethys and the formation of the Adriatic rifted margin. Following Mohn et al. (2012), this process occurred in three stages:

(1) The stretching phase (220-185 Ma), which is linked to the formation of rift basins bounded by widely distributed high-angle normal faults (Eberli, 1988). The related normal faults are typically listric and rooted at mid-crustal levels (Bertotti, 1991). During this stage, extension in the brittle upper crust is decoupled from deformation in the mostly mafic and therefore stronger lower crust. The subcontinental mantle and the lower crust cooled at that time, as recorded by $^{40}Ar/^{39}Ar$ ages on amphibole from the Malenco unit (Hermann et al., 1997; Villa et al., 2000).

(2) The necking phase (185-175 Ma; thinning phase of Mohn et al., 2012) corresponds to the localisation of extension within the future distal margin (Froitzheim and Eberli, 1990), and the continental crust is thinned to ~10 km by the complete obliteration of the ductile middle crust. The Briançonnais domain starts to be uplifted (e.g., Decarlis et al., 2013), and the initially ductile middle crust starts to be exhumed at the seafloor along “necking” faults (Chenin et al., 2019; Mohn et al., 2012).

(3) The exhumation phase (175-165 Ma) initiates when the crust in the distal domain has been thinned below 10 km and is entirely brittle. Detachment faults cut into the lower crust and the mantle enabling its exhumation to the seafloor (e.g., Mohn et al., 2012). The final exhumation faults are cross cutting a crustal section that has been reduced during the previous necking phase.

The final architecture of the distal margin is the result of the superposition of all extensional phases on the inherited pre-rift Permian crust. Rock units that were prior to rifting on top of each other were juxtaposed and occurred at the end of the rifting stage next to each other as a consequence of rift-related thinning and exhumation. The evolution of the thinning and exhumation is documented by the *P–T–t* evolution of these rocks as well as by the syn-tectonic sediments associated with these events (e.g., Petri et al., 2019). In this work, we are mainly focusing on the evolution of the middle crust from the pre-rift Permian stage to the Jurassic rifting stage. These rocks were exhumed in between the distal and the proximal domains, in the so-called “necking” zone, and are today exposed in the Grosina and Campo units.

2.1.3. Alpine reactivation

From Late Cretaceous onward, the Jurassic Adriatic margin was reactivated and disrupted by Alpine convergence. The stacking of the nappes occurred from Late Cretaceous to Tertiary, by multistage thrusting of proximal domains over more distal domains of the margin. The first major deformation phase, the Da1 phase (Trupchun phase of Froitzheim et al., 1994) consists of a W- to NW-directed thrusting occurring between 100 and 76 Ma (see Froitzheim et al., 1994; Handy et al., 1996), and related to the coeval closure of the Meliata-Vardar domain further East and the onset of the closure of the Alpine Tethys (Froitzheim et al., 1996; Mohn et al., 2011). This is followed by the Da2 phase (Duncan-Ela phase of Froitzheim et al., 1994), an extensional phase developing normal faults and associated recumbent folds (Froitzheim et al., 1994) during Late Cretaceous times (80-67 Ma; Handy et al., 1996). The subsequent Da3 phase (Blaisun phase of Froitzheim et al., 1994) is

expressed by large-scale upright open-folds with sub-horizontal E-W trending axis in upper greenschist facies conditions (Hermann and Müntener, 1992). Da3 has been estimated to be Eocene in age and is associated with the continental collision between Adria and Europe, but the recently published ages of Picazo et al. (2019) in the Malenco-Margna nappes shift the prograde metamorphic event to ca. 63 Ma (U-Pb on rutile) followed by a retrogression at ca. 55 Ma (U-Pb on titanite). The complete nappe stack is finally deformed by the Engadine and the Insubric Lines, both related to the Periadriatic fault system.

2.2. The Campo–Grosina units

The study area encompasses the Campo and the Grosina units that are part of the middle Austroalpine units (following Mohn et al., 2011), exposed in SE Switzerland and N Italy. Both units are separated by the sub-horizontal Eita Shear Zone (ESZ) that can be mapped continuously over more than 20 km (Figs 2,3; Meier, 2003; Mohn et al., 2012; Petri et al., 2019).

The hanging wall of the ESZ, the Grosina unit, is essentially made of Bt-bearing orthogneiss (also known as “Cristallino di Grosina”, Figs 3a-d,4ab) associated with garnet-staurolite-bearing metapelite with rare occurrence of andalusite, and crosscut by rare Grt-bearing granodiorite dykes. Orthogneiss is derived from an Ordovician protolith (see Boriani et al., 2005) that is preserved from subsequent deformation phases in a few locations only (e.g., Fig. 4a), and comparable to other pre-Variscan basement units in the Alps (e.g., Strona-Ceneri Zone, Southern Alps; Zurbriggen et al., 1997). The structural evolution of the Grosina unit, although not well constrained yet, involves three main fabrics. (1) A sub-vertical foliation (Sg1) is only locally preserved due to the pervasive overprint during the development of (2) a sub-horizontal planar fabric (Sg2) formed at amphibolite-facies grade associated with a well-defined lineation with a NW-SE trend (Figs 3b,4b), with metric sheath folds in the metasediments. Orthogneiss, metasediment and granodioritic dykes are deformed by local greenschist facies shear zones (Figs 3cd,4c; Petri et al., 2019), notably approaching the ESZ in which chlorite-rich orthogneiss presents (3) a sub-

horizontal Sg3 fabric (Fig. 3d). This new fabric is parallel to the Sg2 fabric and shows a similar NW-SE trending lineation. The complete section is crosscut by undated and undeformed dykes (andesite?), potentially coeval to the ones described in the underlying Campo basement (Bianchi Potenza et al., 1985) and related to the Cenozoic magmatism along the Periadriatic faults system. Mohn et al. (2012) presented the only ages available for the Grosina basement with $^{40}Ar/^{39}Ar$ dating on muscovite, ranging between 273 and 260 Ma (Fig. 10a, Supplementary Material S5 and S7).

The Campo unit, located in the footwall of the ESZ, contains amphibolite-facies metasediments (Fig. 4d) derived from an Ordovician protolith (Bergomi and Boriani, 2012) with paragneiss, micaschist, and minor intercalations of marble and amphibolite. The unit is affected by a metamorphism reaching up to 6 kbar and 650 °C, synchronous with the development of a N-W steeply dipping foliation overprinted by a N-E trending sub-vertical Sc2 fabric (Fig. 3aef; for complete structural description of the Campo unit, see Petri et al., 2018, 2016). Both likely formed during the Variscan orogeny. It was subsequently intruded by several plutons during the Permian (300-270 Ma, U-Pb on zircon and Sm-Ng ages; e.g., Petri et al., 2017; Tribuzio et al., 1999), notably the Sondalo gabbroic complex (Figs 2a,4f) with associated contact metamorphism reaching upper amphibolite to granulite-facies (Fig. 4e; Braga et al., 2001; Petri et al., 2016), and the development of a high-temperature Sc3 fabric at the contact of the complex with the host rocks (Petri et al., 2018). Locally, undeformed Permian pegmatitic dykes crosscut the Sc2 foliation (Fig. 3ef) and were dated at 255-250 Ma (Sm-Nd ages; Sölva et al., 2003). Rb–Sr ages on muscovite from pegmatites and granitoids range between 277 and 251 Ma and between 263 and 97 Ma on biotite (see supplementary Table S5 for references; Fig. 10b). $^{40}Ar/^{39}Ar$ and K–Ar ages from other lithologies are spanning between 217 and 187 Ma for muscovite and from 189 to 122 Ma for biotite (Fig. 10b, Supplementary Material S5 and S7). Hundred meters below the ESZ, the Sc2 planar fabric of the Campo unit is rotated by Fc4 recumbent folding with E-W trending axes and shallow

W-dipping axial planes, affecting also the Permian pegmatites (Fig. 3e). The rest of the Campo unit is little affected by the ESZ-related deformation.

2.3. The Eita shear zone

Both Fc4 recumbent folding in the Campo unit and Sg3 fabric in the Grosina unit intensify approaching the ESZ, and overprint Permian fabrics and pegmatites: the activity of the ESZ is therefore post-Permian (Mohn et al., 2012; Petri et al., 2019, 2018, 2016).

The Campo–Grosina units are thrust during late-Cretaceous (Da1; Froitzheim et al., 1994) by the overlying Filladi di Bormio unit (Fig. 2). This unit is made of prograde greenschist facies metapelites of unknown age (Boriani et al., 2011). At the contact with the Filladi di Bormio, micaschists from the Campo unit are retrogressed into greenschist facies rocks.

The ESZ was previously interpreted as a late-Cretaceous Da1 Alpine thrust (Meier, 2003). However, the ESZ being cross-cut by Da1 thrusts in several locations (Fig. 2) and with new geochronological arguments, Mohn et al. (2012) interpreted this structure as a Jurassic extensional shear zone active during rifting (200–180 Ma) with possible, but only minor Alpine reactivation. The superposition of both units through the activity of the ESZ has therefore been established before the first Alpine deformation occurred (Da1), hence during rifting.

3. Analytical methods

Former geochronological investigations were focused along the contact between the Campo and the Grosina units (Meier, 2003; Mohn et al., 2012) in order to constrain the age of activity of the ESZ. By contrast, the precise characterization of exhumation and cooling history of these units with modern dating techniques are lacking. To this end, we stepped away from the ESZ and selected amphibole, muscovite and biotite grains from various lithologies in both units to carry out petrological characterization and $^{40}Ar/^{39}Ar$ step-heating dating (sample location indicated in Fig. 2, sampling coordinates in Table 1, and Supplementary Tables S2-S4). Mineral abbreviations follow IUGS recommendations after Siivola and Schmid (2007).

3.1. Mineral composition

Major element mineral compositions were determined for dated samples at the Institute of Earth Sciences of the University of Lausanne using a JEOL JXA-8530F HyperProbe EPMA equipped with five WDS detectors, and operating at 15 kV acceleration voltage and 15 nA. Particular attention was paid to the celadonite (Si content) and paragonite (Pg = Na / (Na + K)) substitutions in muscovite and its Ti content that are pressure and temperature sensitive. Biotite was monitored through X_{Mg} = Mg / (Fe_t + Mg) and its Ti content to estimate temperature; and amphibole was monitored through its Al, Na and Ca/K content. Thermobarometric estimates were derived when applicable using the Wu and Chen (2015) Ti-in-muscovite and Henry (2005) Ti-in-biotite thermometers. The Ernst and Liu (1998) thermobarometer based on the Al and Ti content of amphibole was applied to MORB-type lithologies, the Schmidt (1992) Al-in-hornblende barometer was applied to tonalitic lithologies. Measured mineral compositions and calculated thermobarometric estimates are reported in Fig. 5, Table S1, and compiled in Table 1.

3.2. $^{40}Ar/^{39}Ar$ geochronology

Multigrain $^{40}Ar/^{39}Ar$ isotopic analyses were performed on muscovite, biotite, and amphibole by laser step-heating at the Faculty of Earth and Life Sciences, VU Amsterdam. Minerals were separated at the mineral separation laboratory of the Faculty of Earth and Life Sciences, VU Amsterdam after crushing, sieving between 250 and 500 µm and cleaning ultrasonically with demineralized water. Desired minerals were concentrated using a vibrating table, heavy liquids, and a magnetic separator to be finally selected by hand picking under the binocular. Mineral packages wrapped in Al-foil were co-irradiated with DRA sanidine standard packages wrapped in Cu-foil as fluence monitor at the NRG-Petten HFS facility in the Netherlands for 18 hours.

Measurements were performed after ca. 6 months to allow ^{37}Ar decay in Ca-rich amphiboles. Samples were pre-heated to ~ 200 °C to remove undesirable atmospheric argon. Total fusion and step-heating, for standards and samples, respectively, were carried out by a Synrad CO_2

laser combined to a Raylease scan-head system to scan the totality of the mounted grains. Isotopic ratios were evaluated using a MAP 215-50 mass spectrometer with both secondary electron multiplier and Faraday collector. Blanks were measured every two (muscovite and biotite) to four (amphibole) samples measurements and before and after each experiment. Mass discrimination was made through $^{40}Ar/^{36}Ar$ air pipette aliquots measurement.

Ages were calculated using ArArCalc (Koppers, 2002) using the decay constants of Steiger and Jäger (1977), and the atmospheric $^{40}Ar/^{39}Ar$ ratio of 298.56 ± 0.1% (Lee et al., 2006). For each sample, the J irradiation parameter was determined through linear interpolation between each standard. Standard calibration of 24.99 Ma from Wijbrans et al. (1995) was used for VU89 experiments, whereas calibration of 25.42 Ma from Kuiper et al. (2008) was used for experiments VU97D. Raw dating analytical results are provided in Supplementary Table S2 for muscovite, Supplementary Table S3 for biotite and Supplementary Table S4 for hornblende. Results are represented as step-release spectra and inverse isochrons in Figs 6-9, in which errors are reported at 2σ (95% level of confidence), together with the mean standard weighted deviation (MSWD).

Ages are subsequently discussed using Monte Carlo simulations to generate random temperature-time paths used to calculate synthetic argon ages in micas with DiffArgP (Warren et al., 2012a), a version of DiffArg (Wheeler, 1996) that integrates the P-dependency of muscovite diffusion parameters (Harrison et al., 2009), and the diffusion parameters of Harrison et al. (1985) for biotite. A total of 10,000 paths per scenario were generated, defined by 4 nodes for the Grosina unit (G1 to G4) and up to 5 nodes for the Campo unit (C1 to C5). Nodes are located in T-t-P boxes constrained from geological arguments (Fig. 11b) and that may overlap. Each node is randomly picked within a box, with the only rule that age should always decrease (e.g., from node G1 to node G2). For each path, calculated muscovite and biotite bulk ages (cylindrical grains with 0.25 mm radius) were compared to the measured ages through a merit function compiled using the probability density function based on the population of measured ages and associated uncertainties.

Paths reaching high probabilities (p) translate a high fit between the modelled age and the set of measured ages (Fig. 12); paths with $p < 0.05$ were discarded. The model space is also explored by age of key nodes for the temperature-time evolution and key cooling rates (Fig. 12). More details are reported in Supplementary Text S8.

4. SAMPLE PETROLOGY

We selected two samples from the Grosina unit and eight samples from the Campo unit including granodiorite, diorite, amphibolites and metapelites (microphotographs of samples are provided in Fig. 4 and Supplementary Material S6). All samples were selected for having well preserved minerals that crystallized before or during the emplacement of the Sondalo gabbroic complex, and the weakest possible post-Permian deformation microstructures.

4.1. Grosina unit

Two samples were collected from the Grosina unit: *Sample GM119* is a Bt-granodiorite that underwent only minor Dg2 deformation. Quartz presents lobate grain boundaries, but large euhedral and inclusion-free biotite and feldspar preserved their magmatic structure assemblage (Fig. 4a). Biotite grains have a low X_{Mg} (0.37-0.43), with core richer in Ti (0.15-0.21 a.p.f.u.) than rim (0.08-0.18 a.p.f.u.), reaching temperature estimates of 681 ± 16 °C and 617 ± 50 °C, respectively.

Additionally, *sample GM264* is a Bt–Ms paragneiss with minor garnet content with Bt-Ms crystals aligned in the Sg2 foliation alternating with porphyroblastic feldspar. Quartz presents an equant microstructure with numerous pinning structure on mica layers indicative of pervasive static recrystallization. A few muscovite grains present high Si-content (> 3.1 a.p.f.u.) with grain core having a slightly higher Si content than the rim, *Pg* is rather variable (0.07-0.15 a.p.f.u.). The Ti-content of muscovite is low (< 0.03 a.p.f.u.), resulting in similar temperature estimates between cores (578 ± 20 °C) and rims (561 ± 33 °C). Biotite is characterized by low Ti-content (< 0.10 a.p.f.u.) and a moderate X_{Mg} (~ 0.5), with no compositional difference between core and rim; calculated temperature estimate reaches 570 ± 8 °C.

346 **4.2. Campo unit**

347 Three samples of metasediments have been selected from the Campo unit. *Sample CP003b*
348 is a restitic migmatite sampled in the contact aureole of the Sondalo gabbroic complex. The sample
349 presents the Sc3 foliation synchronous to the emplacement of the Sondalo gabbro; muscovite is
350 randomly oriented in quartz-rich levels and appears post-kinematic and post peak metamorphic
351 conditions. Quartz forms polygonal aggregates and presents weak undulous extinction. Muscovite
352 presents a few sillimanite inclusions but no compositional zoning, a high *Pg* (~ 0.13 a.p.f.u.) and Ti-
353 content (0.04-0.07 a.p.f.u.), and a low Si-content (~3.02 a.p.f.u.), constraining a temperature of 691
354 ± 33 °C.

355 *Sample CP028c* is a micaschist collected close to the Sondalo gabbro. Quartz shows very
356 weak development of sub-grain rotation microstructure, whereas plagioclase is not deformed.
357 Porphyroblastic muscovite and biotite are aligned in the Sc2 fabric. They are kinked in places and
358 recrystallized in micrometric grains. Muscovite porphyroblasts have very low *Pg* (~ 0.07) and Si-
359 content (~ 3.00 a.p.f.u.), and rather high concentration in Ti (0.05 a.p.f.u.), without any difference
360 between core and rim. Temperature estimates reach 695 ± 8 °C. Biotite porphyroblasts are
361 homogeneously rich in Ti (~ 0.20 a.p.f.u.) and have a moderate X_{Mg} (~0.46), constraining a
362 temperature of 698 ± 16 °C.

363 *Sample CM260* is a Grt-Ms-Bt micaschist with Ms-Bt aggregates aligned in the main pre-
364 Permian Sc2 fabric of the Campo basement. Micas are inclusion-free, and a few large biotite
365 crystals are included in garnet. Biotite is locally slightly chloritized, but quartz presents equant
366 textures and is pinned to micas grains. Muscovite grains have moderately low Si (3.04 a.p.f.u.) and
367 Ti (0.03 a.p.f.u.), and high *Pg* (0.14-0.16) with rims being slightly richer in *Pg* than cores.
368 Temperature estimates are 572 ± 32 °C for cores and 562 ± 44 °C for rims. Biotite has low X_{Mg} (~
369 0.40) and Ti (0.12 a.p.f.u.), without presenting compositional difference between core and rim;
370 temperature estimates reach 611 ± 14 °C.

*T*wo amphibolites were selected. *Sample CP010g* presents hornblende aligned in the pre-Permian Sc2 fabric. Quartz and plagioclase are present in polygonal aggregates, whereas isogranular amphibole composition points to a magnesio-hornblende, with low Al-, Na- and Ti-content (Al^{tot} = 1.99 a.p.f.u., Na^{M4} = 0.14 a.p.f.u. and Ti = 0.07 a.p.f.u., respectively), high Ca/K ratio (~ 31) and no difference between core and rim. In the lack of proper mineral assemblage, no thermobarometric estimates were performed.

Sample CM234 is an amphibolite with hornblende aligned in the Sc2 fabric too, but in the vicinity of the ESZ. Amphibole is euhedral and forms continuous beds separated by plagioclase aggregates, both showing no evidence for dynamic recrystallization. Amphibole composition is a tschermakitic to magnesian hornblende, with moderate Al- content (Al^{tot}= 2.30 a.p.f.u.) and low Na- and Ti-content (Na^{M4} = 0.10 a.p.f.u., Ti = 0.08 a.p.f.u.), with no difference between amphibole core and rim. The rock assemblage does not allow for proper thermobarometeric estimates.

Finally, three magmatic rocks from the Sondalo gabbroic complex were selected. *Sample CP031a* is a garnet-bearing granodiorite collected at the margin of the Sondalo gabbroic complex. The rock preserves its magmatic structure and mineralogy, with subhedral plagioclase and biotite and xenomorphic amphibole. Thin polygonal quartz aggregates lie along plagioclase grain boundaries with no evidence for sub-solidus deformation. Amphibole contains in places biotite inclusions and has a composition of a ferro-tschermakitic hornblende with Al-poor and Ti-rich cores (2.29 a.p.f.u. and 0.09 a.p.f.u., respectively) compared to rims (2.67 a.p.f.u. and 0.05 a.p.f.u., respectively), with a homogeneous Ca/K ratio (~ 21). Cores are slightly richer in Na (Na^{M4} = 0.19) than rims (Na^{M4} = 0.16). The application of the Schmidt (1992) barometer constrains a P estimate of 9 kbar (Table 1). Biotite contains a few inclusions of opaque minerals, is not zoned and has a low Ti-content (0.07-0.14 a.p.f.u.) and moderate X_{Mg} (0.44), pointing to a temperature of 581 ± 40 °C. This temperature estimate is slightly off the range of temperature of the calibration of Schmidt (1992), and the resulting pressure is higher than what was estimated in Petri et al. (2016).

Sample CP032c is an amphibole-bearing gabbro from the centre of the Sondalo gabbro, preserving a poikilitic magmatic structure with interstitial amphibole rimming pyroxene cores with magnetite inclusions. Amphibole is an iron-rich pargasite, with a high Ti-content (Ti = 0.34 a.p.f.u.), and a moderate Na- and Al-content (Na^{M4} = 0.25 a.p.f.u., Al^{tot} = 2.29 a.p.f.u.). Conditions of equilibration of the amphibole are constrained by the Ernst and Liu (1998) thermobarometer to 950 °C for 6 kbar, in agreement with Petri et al. (2016).

Sample CP034c is a granodiorite from the centre of the Sondalo gabbro sampled close to a metapelitic xenolith. It contains large euhedral garnet and subhedral biotite and plagioclase showing a preferred orientation: the preservation of magmatic minerals and the absence of evidence for sub-solidus recrystallization indicates that the fabric formed at supra-solidus conditions. Biotite grains show no compositional difference between core and rim, with low Ti (0.07-0.08 a.p.f.u.) and high X_{Mg} (0.60-0.62), constraining a temperature of 563 ± 10 °C.

5. ARGON DATING

In most cases, the analytical data were too disturbed to define “plateau” ages that normally require at least three consecutive steps within their 2σ errors encompassing more than 70% of the total released ^{39}Ar: sub-plateau were defined by correlating the age spectrum and the estimated K/Ca ratio of each step. In case of suspected excess argon shown e.g., by older steps in the beginning of the spectrum, the inverse isochron method was used, allowing the identification of the extraneous source of argon. We analysed muscovite (Fig. 7) and biotite (Figs 8,9) from both the Campo and the Grosina units. In the absence of amphibole-bearing lithologies in the Grosina unit, amphiboles (Fig. 6) were only dated in the Campo unit.

5.1. Grosina unit

5.1.1. Muscovite ages

Muscovite GM264. The highly disturbed step-release spectra give a total age of 262 ± 3 Ma with a very high Mean Standard Weighted Deviation (MSWD). The inverse isochron age reaches 261 ± 2 Ma (Fig. 7a), and is preferred over the step-release spectra.

5.1.2. Biotite ages

Biotite GM119. Eight out of 14 measurements define a "sub-plateau" at 280 ± 3 Ma (Fig. 8a). Measurement points are reasonably well grouped close to the $^{36}Ar/^{40}Ar = 0$ line in the inverse isochron age but present a trend pointing to excess argon. Moreover, ages are decreasing with the increasing laser power usually indicating biotite–chlorite intermixing resulting in ^{39}Ar recoil from biotite to chlorite during irradiation (e.g., Lo and Onstott, 1989). However, the chlorite content here is likely too low to be identified with high $^{37}Ar/^{39}Ar$ ratios. It is therefore recommended to use the inverse isochron age of 246 ± 13 Ma.

Biotite GM264. Fifteen of the 21 steps define a sub-plateau at 246 ± 1 Ma, coeval with the total fusion age (Fig. 8b). As the spectrum is quite disturbed, the isochron age of 245 ± 2 Ma should be used rather than the "plateau" or total fusion age.

5.2. Campo unit

5.2.1. Amphibole ages

Hornblende CP010g. Isotopic measurements show strong excess ^{40}Ar in the mineral (Fig. 6a) with hardly realistic ages. Both total fusion age of 510 ± 4 Ma and inverse isochron age of 283 ± 90 Ma are geologically meaningless due to the high excess argon content.

Hornblende CP031a. The spectrum is highly disturbed, with old ages in the beginning of the experiment, decreasing down to 183.50 Ma for the last step. More than 40 % of the released ^{39}Ar constitute steps older than the age of emplacement of the Sondalo gabbro determined by U-Pb on zircon (Fig. 10; Petri et al., 2017), confirming a strong component of excess argon (Fig. 6b). On the

inverse isochron plot, data are moderately aligned between air and a single radiogenic reservoir: the mean inverse isochron constrains an age of 205 ± 9 Ma, and data can be bracketed between an old and a young envelope with inverse isochron ages of 210 ± 4 Ma and 177 ± 13 Ma, respectively.

Hornblende CP032c. Isotopic measurements show strong excess ^{40}Ar (Fig. 6c); the total fusion age of 493 ± 4 Ma, the inverse isochron age of 344 ± 8 Ma and every single measurement step are older than the emplacement age of the Sondalo gabbroic complex determined by Sm–Nd or U–Pb (Fig. 10), pointing to unrealistic ages.

Hornblende CM234. Isotopic measurements show strong excess ^{40}Ar in the mineral (Fig. 6d) with continuously decreasing step ages. Both total fusion age of 493 ± 4 Ma and the inverse isochron age of 135 ± 20 Ma constrained by very scattered data points are geologically meaningless.

5.2.2. Muscovite ages

Muscovite CP003b. Five consecutive steps out of 13 steps constrain an age of 217 ± 2 Ma close to the total fusion age of 216 ± 2 Ma (Fig. 7b). Data are very scattered on the inverse isochron plot suggesting a strong mixing between air and radiogenic argon, indicating an age of 218 ± 2 Ma. This may suggest weathered muscovite (e.g., illitization; de Jong et al., 2001) but with only air mixed with one radiogenic ^{40}Ar source; the inverse isochron age should hence be preferred.

Muscovite CM260. Eighteen consecutive steps loosely define an age of 182 ± 2 Ma, coeval with the total fusion age of 182 ± 1 Ma (Fig. 7c). Inverse isochron confirms that the sample contains only one argon reservoir with a minor air component and gives an age of 182 ± 2 Ma that is preferred over the step-release spectrum.

Muscovite CP028c. The first 4 consecutive steps loosely define an age of 176 ± 4 Ma, with a total fusion age of 178 ± 2 Ma (Fig. 7d). On the inverse isochron, data are well grouped and define an age of 178 ± 5 Ma. In the view of the disturbed step-released spectrum, the inverse isochron age is preferred.

5.2.3. Biotite ages

Biotite CP034c. Ages become progressively older during the experiment, pointing to a partial argon loss. Eight out of 14 steps define an age of 216 ± 2 Ma, with a total fusion age of 212 ± 2 Ma (Fig. 8c). The inverse isochron plot shows scattered data points, with an inverse isochron at 214 ± 3 Ma. The inverse isochron age is preferred to the sub-plateau age, because of the high MSWD of the latter.

Biotite CP031a. Seven consecutive steps selected from 14 steps constrain a reasonable plateau of 173 ± 2 Ma with a MSWD = 0.7, totalling more than 70 % of the released ^{39}Ar (Fig. 8d). Despite the spread of data in the inverse isochron diagram, the plateau age is reasonable. The total fusion age is 170 ± 2 Ma and the inverse isochron age is 171 ± 2 Ma. The plateau age is therefore preferred.

Biotite CM260. Six out of 20 steps defines a "sub-plateau" age of 171 ± 1 Ma close to the total fusion age of 172 ± 1 Ma and preferred over the inverse isochron age of 171 ± 2 Ma (Fig. 9a). Both the inverse isochron plot pointing to a quite strong contribution of air in the biotite and the decreasing age indicate that biotite is slightly chloritized (Lo and Onstott, 1989), in agreement with petrographic observations. This is however not identified by the ^{37}Ar/^{39}Ar ratio of these steps due to ^{37}Ar concentrations below detection limits.

Biotite CP028c. Ten consecutive steps out of 14 steps define a sub-plateau age of 174 ± 2 Ma (MSWD = 8) and a total fusion age of 173 ± 3 Ma (Fig. 9b). The inverse isochron presents scattered data but with a consistent age of 174 ± 2 Ma. The plateau age is here preferred.

6. DISCUSSION

6.1. Significance of measured ages

6.1.1. Muscovite ages

Dated muscovite from the Campo unit have a large *Pg* and Ti compositional range, pointing to various temperatures of equilibrium, as confirmed by the thermometry calculations

(Table 1). Despite variable composition, ages of muscovite CM260 and muscovite CP028c are similar within error. This is however not the case for muscovite CP003b that is 30 Myr older, with an identical Si and Ti content, and a *Pg* between the two other samples. All muscovite grains are, however, not occurring in the same structural position: the older muscovite CP003b is growing post-deformation and post-peak metamorphic conditions in a quartz-rich layer. Conversely, the two other samples present grains that crystallized before or during Permian times based on the following elements: (1) both CM260 and CP028c samples have preserved muscovite grains aligned in the Sc2 fabric that predates the intrusion of the Sondalo gabbroic complex, (2) muscovites show no microstructural evidence for recrystallization in CM260, and only large porphyroclasts were selected in CP028c, and (3) muscovite still preserves its peak-metamorphic compositions as attested by applied thermometry (695 °C and 567 °C, respectively). This is in line with estimates obtained by biotite thermometry (see below) as well as for the regional and contact metamorphism around the Early Permian Sondalo gabbro (Petri et al., 2017, 2016). These temperature estimates are notably above the expected closure temperature of the argon system in muscovite. Therefore, the overlapping 182 and 178 Ma ages of muscovite CM260 and muscovite CP028c can be interpreted as cooling ages. This is not straightforward for the older muscovite CP003b that can also be interpreted as a crystallization age given its structural position. Interestingly, this 217 Ma age is coeval to the older ages of amphibole in the lower crustal Malenco unit (Villa et al., 2000), pointing to a potential role of deformation-induced fluid mobilization during early rifting stages. An alternative scenario would be that the older muscovite ages are caused by a strong component of extraneous argon, related to the Permian emplacement of the Sondalo gabbro.

The age of muscovite GM264 from the Grosina unit is clearly different than the age of muscovite CM260 and muscovite CP028c from the Campo unit, highlighting an age contrast between the two units. In both units, mineral compositions are variable and not correlated with ages. Step-release spectra are rather disturbed for all dated muscovite grains, notably from the Grosina

unit. Yet, the inverse isochron plot presents rather clustered measurements, pointing to systematic single radiogenic argon reservoirs, with low air contamination thus validating the various ages.

6.1.2. Biotite ages

Three of the four biotite ages from the Campo unit lie in the 174-171 Ma range; biotite CP034c appears as an outlier age, evaluated at 216 Ma. All samples present either the pre-Permian Sc2 fabric (biotite from micaschists CM260 and CP028c), or preserve Permian magmatic textures, microstructures (biotite from igneous CP034c and CP031a). The equilibrium temperature estimates based on biotite composition are overlapping with muscovite thermometry for the two metasediments (611 °C and 698 °C for CM260 and CP028c, respectively; Table 1), and are consistent with estimates from Petri et al. (2016). The biotite temperature estimates for the two granodiorites (581 °C and 563 °C) are lower than expected for the crystallization temperature of biotite for such melt composition. This is very likely due to the fact that Henry (2005) Ti-in-biotite thermometer was calibrated with metapelites only. For all samples, biotite thermometry reaches temperatures largely above the expected closure temperature of the argon system in biotite. The three youngest samples encompass the full range of biotite composition, showing that such mineral compositions had no effect on apparent argon retention. This is however not the case for the older biotite CP034c that was separated from a Permian granodiorite, and not from a metasediment; it has the composition of a phlogopite with much higher X_{Mg}, likely caused by a higher bulk rock Mg-number. This strong compositional difference may increase argon retention, increasing in turn the closure temperature for the biotite grains of this sample (potentially a few tens of °C; Harrison et al., 1985). This effect of biotite composition on Ar retention is, however, not identified for annite-rich biotite (X_{Mg} below 0.5), in agreement with Grove and Harrison (1996). Based on the structural control, the preserved high-temperature mineral textures and compositions, we can state that all biotite ages from the Campo unit can be interpreted as cooling ages, but with a potentially higher

541 closure temperature for sample CP034c. Alternatively, this older age for CP034c can be due to
542 incorporation of extraneous Ar, as discussed hereafter.

543 Regarding the Grosina unit, both biotite ages are coeval at 246-245 Ma. Related grains are
544 occurring in two different and likely not coeval structural contexts, minerals being either aligned in
545 Sg2 (micaschist GM264) or still preserving magmatic biotite from the granitic protolith
546 (orthogneiss GM119). Temperatures estimated from both biotite and muscovite of sample GM264
547 are notably identical (569 °C and 570 °C, respectively). Derived ages are therefore interpreted as
548 cooling ages. Measured biotite have variable Ti-content but rather low X_{Mg}, similar to biotite from
549 the Campo unit (except biotite CP034c). Therefore, a simple difference in mineral composition does
550 not explain the observed difference in age between the Campo and the Grosina units.

551 ***6.1.3. Amphibole ages***

552 Whereas hornblende CP032c reaches pressure estimates consistent with previous works,
553 hornblende CP031a leads to slightly higher P that may be caused by a high-Al bulk rock
554 composition compared to the tonalitic calibration of Schmidt (1992), which is also attested by the
555 presence of Grt in this sample. The paragenesis of the two other amphibole-bearing samples,
556 however, excluded the use of Al-in-hornblende barometry. Despite structural and metamorphic
557 control, most amphibole ages led to meaningless ages, being strongly affected by extraneous argon
558 contamination. Among the four, only hornblende CP031a was prone to derive a geologically
559 relevant age using the inverse isochron, bracketed between 210 ± 4 and 177 ± 13 Ma.

560 ***6.1.4. Possible reasons for excess ^{40}Ar***

561 The assumption that the argon system was initially open and above the “closure
562 temperature” is expected to be valid for long term residence in the middle and lower continental
563 crust for standard temperature and pressure condition (e.g., Warren et al., 2012b). We however
564 noticed that several of our samples present excess-Ar based on several points: (1) amphibole
565 sampled in but also around the Permian Sondalo gabbro have older $^{40}Ar/^{39}Ar$ ages than the age of

intrusion of the pluton determined by U–Pb on zircon and Sm–Nd ages (Fig. 10b; Petri et al., 2017; Tribuzio et al., 1999), (2) amphibole systematically presents dates decreasing during the experiments with increasing $\%^{39}Ar$ released, and (3) amphibole have moderately to highly scattered measurement points in inverse isochron plots. The two older mica ages recovered from the Campo unit (muscovite CP003B and biotite CP034c) may also be older by excess argon, although alternative scenarios are also plausible (see discussion above).

We suggest that the high $^{40}Ar/^{36}Ar$ ratio of the Sondalo gabbro original melt is the first possible source of excess-Ar in the pluton and its country rocks: excess-Ar was mobilized due to heat introduced into the unit by the mantle-derived mafic intrusion that disturbed $^{40}Ar/^{39}Ar$ ratios. As the melt sources in mantle partial melting, it has a low K-content and associated low radiogenic Ar production. Its $^{40}Ar/^{36}Ar$ ratio is consequently very close to the high ratio of the mantle (e.g., Staudacher et al., 1989). The second possible source may be related to the intrusion of such a melt in a K-rich environment. Although Ar is expected to leave and diffuse out of the mineral, the higher environmental Ar inhibited this process and potentially triggered back diffusion from the external reservoir into the mineral. This process was documented in country rocks few meters around intrusions (Hyodo and York, 1993). However, in the Campo unit, disturbed analyses are located up to 5 km away from the intrusion, questioning the extent of the gabbro below the nowadays exposed surface of the Campo unit, or the ability of a postulated excess ^{40}Ar “wave” to affect host rocks.

Micas are expected to be more affected by extraneous argon incorporation due to the higher partition coefficient between extraneous fluids and micas (Kelley, 2002) compared to amphibole. The amphiboles of the Campo unit were, however, significantly more affected by excess-Ar than the micas. This is likely due to the more sensitive character of amphibole caused by a low ^{40}K content and therefore a lower internal radiogenic ^{40}Ar concentration (Kelley, 2002). In addition, this extraneous ^{40}Ar contamination occurred at a time micas were still residing above their closure conditions. Only muscovite CP003b and biotite CP034c, being ca. 30 Myr and ca. 40 Myr

older than other dated muscovites and biotites from the Campo unit are potentially retracing this high, inherited $^{40}Ar/^{36}Ar$ ratio. In this scenario, the older "sub-plateau" age presented in Figures 7b and 8c may be due to extraneous ^{40}Ar incorporation homogeneously distributed in the mineral lattice (Foland, 1983) potentially brought by fluids (Kelley, 2002).

6.2. Age difference between the Campo and the Grosina units

The Grosina and the Campo units apparently underwent contrasting evolutions (Fig. 10). The Grosina unit shows consistent muscovite ages between 273 and 261 Ma older than the biotite ages at 248–246 Ma. By contrast, the Campo unit has a poorly constrained amphibole age (between 210 ± 4 and 177 ± 13 Ma) partly overlapping muscovite ages spanning between 182 and 176 Ma. Similar muscovite ages of the Campo unit further south were dated by Meier (2003) at 188 ± 4 Ma. Dated biotite separates from the Campo unit are slightly younger, ranging between 174 and 171 Ma (± 1–2 Ma). Figure 10ab clearly illustrates that the Campo unit has ages significantly younger than the Grosina unit. The transition between the two basement units, marked in the field by the ESZ, is characterized by a sharp change in $^{40}Ar/^{39}Ar$ ages (Fig. 10c). In both units, dated minerals were separated from high-temperature assemblages inferred to be at least Carboniferous or Permian in age. In agreement with petrological and structural considerations, we consider these ages record the cooling rather than the crystallization of minerals.

6.3. Cooling and exhumation history of the Campo and Grosina basements

These new ages, together with a compilation of published U–Pb, Sm–Nd, Rb–Sr, K–Ar and $^{40}Ar/^{39}Ar$ ages performed on both the Grosina and Campo basements (see Fig. 10, Supplementary Material S5 and S7), constitute a consistent dataset to estimate the respective cooling history of the two units. Deciphering the thermal history and cooling rates is hampered by the fact that closure temperatures are sensitive to the cooling rate itself, mineral composition, and grain size. To a first approximation, geochronological data can be linked to the closure temperature of the probed chronometer/mineral system (details presented in Supplementary Figure S7). Two

distinct events of cooling can be identified (Fig. 10 and Supplementary Material S7): a Permo-Triassic cooling, and a subsequent Jurassic cooling. We characterized these two cooling events using a Monte Carlo -based approach (Figs 11,12).

6.3.1. Thermal evolution during Permian post-orogenic extension

From our dataset, the Permian cooling phase is best recorded in the Grosina unit with the 261 ± 2 Ma muscovite age, and the 246 ± 13 and 245 ± 2 Ma biotite ages, indicating a cooling during Permo-Triassic times. At a regional scale, this period corresponds to the end of the intense magmatic and metamorphic event immediately following the Variscan orogeny and its collapse (Fig. 13ab; Petri et al., 2017). This period is associated with the emplacement of both mafic and felsic intrusives from the lower continental crust to the upper continental crust (Hermann and Rubatto, 2003; von Quadt et al., 1994), and regional high-temperature metamorphism (see compilation in Fig. 11; Hermann and Rubatto, 2003; Petri et al., 2016). The cessation of the HT regional conditions implies a progressive thermal relaxation and deepening of the isotherms that caused a thermal subsidence permitting the deposition of Triassic shallow-marine sediments (Fig. 13c; Eberli, 1988).

These constrains were used to design the temperature-time paths of the Grosina unit used as entry values for Monte Carlo DiffArgP simulations (Fig. 11). An Early Permian node G1 is located at 550 ± 150 °C and 3 kbar that is expected to be the thermal maximum of the Grosina unit based on the mineralogical assemblage and the presence of andalusite in the metapelites that are interpreted to be Permian in nearby Austroalpine basement units (Petri et al., 2016; Schuster and Stüwe, 2008). Node G1 is followed by node G2, marking the end of the Permian cooling. The age and temperature of this stage is largely unknown and we opted to evaluate several plausible paths within a broad thermal window (230 ± 30 Ma, 250 ± 150 °C). The period from the middle Permian to the end of the Triassic is characterized by a slow and progressive drowning of the continental surface, indicating that no major tectonic deformation occurred (no major crustal thinning). This

implies that continental basement units were likely not exhumed. As a consequence, we maintain P constant at 3 kbar. Node G3 simulates final rift-related exhumation close to the surface (170 ± 10 Ma, 100 °C, 0.5 kbar). The selected timing is based on both stratigraphic and thermochronological data documenting the evidence for final rifting stage and basement exhumation (Mohn et al., 2010; Müntener and Hermann, 2001; Petri et al., 2019). Node G4 at 0 Ma has similar P-T conditions than node G3.

The 10,000 paths that were generated (Fig. 12a) converge around 260 Ma and around 240 Ma, but are not converging for node G3 because of its large difference in age with our dataset combined to the low T-t gradient of the path. The initial temperature conditions are consistent with qualitative P-T estimates of 550-600 °C that can be deduced from the regional presence of andalusite of probable Early Permian age in the Grosina unit. Although the highest best fit is found for a variable age of node G2 (245-215 Ma), the calculated cooling rate is very constant at 5-10 °C/Myr (Fig. 12a); the highly variable age of node G2 translates a low difference in cooling rates towards the Jurassic node G3.

The Permo-Triassic cooling event can also be reported in the Campo unit using chronometers with higher closure temperatures (Supplementary Figure S7). The difference between Sm–Nd and Rb–Sr ages (11 and 34 Myr of difference for samples SO5/11 and SO5/1, respectively) from the Campo unit led Tribuzio et al. (1999) and Braga et al. (2001) to conclude that rocks from the Sondalo gabbro cooled slowly at a rate of 10 °C/Myr after its emplacement during the Permian. This is confirmed by the Rb–Sr ages on muscovite being 14 Myr older than Rb–Sr ages on biotite (sample PB2 of Del Moro and Notarpietro, 1987) and 35 Myr older than K–Ar ages on muscovite (sample 10-M of Hanson et al., 1966). The spread of Rb–Sr ages may also support a slow cooling (see Fig. 10b), but mixed ages caused by subsequent partial reopening cannot be excluded. The cooling history of the Grosina basement is only documented by $^{40}Ar/^{39}Ar$ dating with a gap of 16 Myr between muscovite and biotite from the sample GM264 (Figs 7a,8b). Although old age pairs

are pointing to fast cooling immediately after the emplacement of the Sondalo gabbroic intrusion, post-intrusion cooling rates for samples collected in the Grosina and the Campo units are below 10 °C/Myr (sample 10-M of Hanson et al., 1966 and GM264). We can thus conclude that the Campo–Grosina units record the same cooling "event" in Permian to Triassic times, which has some implications for the subsequent thermal history (see discussion below).

The low cooling rates here reported (5-10 °C/Myr) are in the same order of cooling rates that are expected during the Permian event (~ 5 °C/Myr; Schuster and Stüwe, 2008). They are also similar to those reported from middle to lower crustal units from the Southern Alps (~ 1-5 °C/Myr in the Ivrea-Verbano Zone; Hurford, 1986; Siegesmund et al., 2008; Wolff et al., 2012), although there, the cooling may have been slowed down by Triassic magmatism as well as by tectonically- and magmatically activated re-heating during the Jurassic (see discussion below).

Cooling can be the result of several tectonic events. The first hypothesis is related to a crustal thinning and exhumation associated to the opening of the Meliata oceanic domain that occurred at around 240 Ma (Stampfli and Kozur, 2006). This is yet unlikely, as the initiation of our cooling (node G1) clearly pre-dates Meliata opening, and Triassic extensional deformation remains very limited in our study area. The second hypothesis is related to a post-orogenic thermal equilibration. The same type of rather low cooling rates has been retrieved by modelling the Mesozoic thermal subsidence of the Paris basin, that lies on the European plate outside the Alpine domain and that did not undergo Jurassic rifting (Prijac et al., 2000): at around 2-4 °C/Myr in the lower continental crust, and 1-3 °C/Myr in the middle crust (considering the first 60 Ma after thermal maximum only). We therefore suggest that our Ar-Ar cooling ages from the Grosina unit records this slow thermal equilibration of the lithosphere after the Variscan orogeny. This cooling implies a thickening of the lithosphere that will progressively subside without faulting at the surface (McKenzie, 1978). This subsidence permitted the deposition of thick continental Permo-Triassic sediments progressively superseded by marine sediments. Cooling rates below 10 °C/Myr seem

characteristic to post-orogenic deep crust recording conductive (isobaric) lithospheric cooling, as reported for Proterozoic orogens (< 10 °C/Myr; Blackburn et al., 2011; Busch et al., 1996; Schmitz and Bowring, 2003; Scibiorski et al., 2016), and rarely documented but similar for Phanerozoic orogenic deep crust (~1-20 °C/Myr; Bohlen and Mezger, 1989; Grove and Harrison, 1999; Hurford, 1986; Siegesmund et al., 2008; Wolff et al., 2012). In addition, these values are significantly low compared to those of deep crust undergoing syn-orogenic exhumation (isothermally decompressed lower crust showing values in the range of 25-100 °C/Myr; e.g., Štípská et al., 2004). The rate of the conductive cooling of the lower crust appears noteworthy one order of magnitude smaller than what can be calculated for a cooling oceanic lithosphere using results of Stein and Stein (1992; averaging the first 60 Myr of cooling), even if tuning the crustal thermal conductivity to continental values (2.5 $W.m^{-1}.K^{-1}$).

The observed cooling rates suggest that isobaric/conductive cooling is more important than faster cooling associated to tectonic exhumation. This statement may however not be valid for shallower crustal levels located in the footwall of Permian extensional detachment faults (Pohl et al., 2018).

6.3.2. Thermal evolution during Jurassic rifting

From our $^{40}Ar/^{39}Ar$ dataset, the Jurassic, rift-related cooling seems to be only recorded in the Campo unit. The new hornblende, muscovite and biotite ages presented in this study span a narrow temporal range within ca. 4 Myr between hornblende and biotite (sample CP031a) and between muscovite and biotite (sample CP028c). It points to a cooling of the Campo basement during the Jurassic that appears to be rapid, with estimates based on theoretical closure temperatures reaching up to 30-45 °C/Myr (Supplementary Figure S7). Such rapid cooling is also indicated by the near-constant age of consecutive steps for biotites, translated by lower MSWD values of the sub-plateau ages for the Jurassic cooling (Campo unit) compared to the Permian cooling (Grosina unit; Figs 7,9). We better constrained the temperature-time evolution of the Campo unit by testing

two scenarios built from regional constrains (Fig. 11). Rifting related to the Alpine Tethys opening initiates during Norian to Late Sinemurian (stretching phase of Mohn et al., 2010) with the formation of high-angle normal faults in the upper crust (Ortler unit; Eberli, 1988), pre-dated by the first Ar-Ar ages in the underlying lower crust and mantle, that is interpreted as the initiation of their exhumation and related deformation (Villa et al., 2000). This leads us to define a model initiation at 250 Ma (node C1), before Jurassic rifting initiated. At that time, the temperature is inferred to be above muscovite expected closure temperature (500 ± 100 °C) at a depth constrained by pre-rift metamorphic conditions in the Campo unit (Petri et al., 2016). Deformation starts being localized in the future necking zone and distal domain at 190-175 Ma (Mohn et al., 2012; Ribes et al., 2020), the youngest pre-tectonic sedimentary deposit in the distal domain (before rift localization) being the Agnelli Formation in the Err-Bernina units (185 Ma). This constrains the initiation of the final exhumation and related cooling at node C3 (185 ± 15 Ma; 450 ± 150 °C; 3 kbar). Deformation in the necking zone is expected to stop at ca. 170 Ma, and hyperextension takes over as the mantle is exhumed in the distal domain at ca. 165 Ma (Müntener and Hermann, 2001; Villa et al., 2000). We therefore propose that at 160 Ma, the deformation and cooling history of the necking zone is ended, constraining a node C4 at 170 ± 10 Ma, 100 °C and 0.5 kbar, and a node C5 at 0 Ma and similar conditions than node C4. The evolution between node C1 and node C3 is however rather unconstrained, as the thermal history of the necking zone involves cooling potentially interrupted by heating phase(s). This is suspected for instance in the Ivrea-Verbano Zone (Southern Alps; Ewing et al., 2015; Smye and Stöckli, 2014), potentially helped by synchronous magmatism (e.g., Galli et al., 2019). The age and temperature increase of such pulse(s) are, however, unknown. A regional thermal peak should be reached before 175 Ma, which corresponds to the period during which the Briançonnais domain and the necking domains are uplifted and emerged (Decarlis et al., 2017; Mohn et al., 2012; Ribes et al., 2020). The oldest bound of this thermal pulse may correspond to the time when the lower crust and the mantle started to rise between 220-190 Ma (Fig. 11). We

741 therefore designed a node C2 at 205 ± 15 Ma, 300 ± 100 °C, and 3 kbar. To test if a re-heating is
742 required, this node C2 is set inactive in a first scenario (Fig. 11 and Fig. 12b; simple cooling from
743 node C1 to node C3, followed by exhumation-related cooling from node C3 to node C4), and is
744 activated in a second scenario to force re-heating from node C2 to node C3, before final exhumation
745 and related cooling from node C3 to node C4 (Fig. 11 and 12c). Each scenario was explored by
746 10,000 individual paths (Fig. 12). The only interpretable amphibole age (hornblende CP031a)
747 carries a large uncertainty, and has therefore been excluded from the rest of the discussion.

748 Both scenarios for the Campo unit clearly converge for node C3 at around 180-175 Ma for
749 400-450°C when the final cooling is initiated and the distribution of path's probability points to an
750 achievement of cooling from 175 to 160 Ma. This indicates that our dataset is clearly supporting a
751 final cooling initiated between 180-175 Ma, with rather fast cooling rates of 25-100 °C/Myr (Fig.
752 12bc). This age slightly precedes the cessation of activity of necking detachment faults and a
753 drowning of the Tethyan necking zones reported from several studies (Southern Alps: Decarlis et
754 al., 2017; Eastern Alps: Mohn et al., 2012; External Crystalline Massifs: Ribes et al., 2020) that
755 occurred in Toarcian-Aalenian times.

756 The thermal evolution of the necking zone before node C3 remains more ambiguous. Our
757 Monte Carlo simulations do not converge for both nodes C1 and C2 (when active, Fig. 12c). We
758 know that the maximal temperature of node C3 should be likely limited, as petrological
759 observations from the Campo unit do not report any evidence from syn-rift high temperature
760 metamorphism, but the initial temperature (position of node C2) and the amount of heating cannot
761 be directly constrained. However, the Campo unit also underwent the Permo-Triassic cooling of the
762 lithosphere (nodes C1 to C2 in scenario 2, Fig. 12c), which is supported by other geochronometers
763 than $^{40}Ar/^{39}Ar$ (see discussion above) and that, considering the pre-rift depth of the unit, should lead
764 to pre-rift temperature slightly above the temperatures of the Grosina unit (~200-300 °C). Such
765 range of temperatures is not permitted by the scenario 1 as pre-rift temperatures are kept high

during the Permo-Triassic (nodes C1 to C3 in Fig. 12b). Hence, the scenario 2 with the presence of a node C2 is favoured. This suggests that a syn-rift heating of basement rocks in the necking zone has occurred, but the maximum temperature (node C3) remains limited to 400-450 °C and the amount of re-heating (nodes C2 to C3) to maximum 200 °C. The re-heating should be achieved by 180 Ma, which is the maximal best-fit age of node C3: this 180 Ma limit is also reported from the Southern Alps necking zone by Beltrando et al. (2015). The potential effect of thermal blanketing expected by thick sedimentary deposits (e.g., Mauléon basin, Pyrenees; Lescoutre et al., 2019; Saspiturry et al., 2020) can here be excluded to cause this heating because of a strong sediment starvation. This heating may instead concomitantly result from the rise of the asthenosphere due to rifting, from the ascent of the lower crust in the adjacent future distal domain (Fig. 13e), and from the activity of deeper extraction faults (see Petri et al., 2019 for details). It may also result in a thermal support allowing to transiently exhume above sea-level pre-rift sediments as reported from the Southern Alps by Decarlis et al. (2017) and potentially basement rocks as suspected in the Mont Blanc massif by Ribes et al. (2020) during the Sinemurian-Pliensbachian (~190-185 Ma). This indicates that the necking zone uplift or even emersion is caused by a flexural response of the lithosphere to rifting (Chenin et al., 2020), but may also be thermally supported.

Noteworthy, the two older ages in the Campo unit (218 ± 2 Ma muscovite age and 214 ± 3 Ma biotite age) can be explained in this scenario either (1) by the preservation of cooling ages from the Permo-Triassic cooling phase (path from nodes C1 to C3), (2) by an increased argon retentivity in biotite due to its high Mg-content but no difference in muscovite composition has been detected for the sample with older muscovite age, (3) by a crystallization that may have occurred close to the argon closure temperature, or (4) by cryptic and homogeneous extraneous argon incorporation.

6.4. Age of the Eita Shear Zone (ESZ)

In contrast to the Permo-Triassic cooling history of the Grosina unit, the final cooling of the Campo unit was achieved during Jurassic necking. The associated fast cooling rates (25-100

°C/Myr) are characteristic of mid-crustal units affected by rift-related exhumation of rocks to shallow and cooler crustal levels (e.g., Beltrando et al., 2013; Bertotti et al., 1999; Decarlis et al., 2017). The presence of brittle deformation structures along the Grosina detachment indicates that the Grosina unit was in the top few kilometres of the crust at the time necking occurred. The pre-rift position and syn-rift evolution of the Campo and the Grosina units can also be discussed following their thermal evolution. The Grosina unit was very certainly below ~ 330 °C before rifting started (below the $^{40}Ar/^{39}Ar$ closure temperature of biotite). The contrasted thermal evolution of the Grosina unit and the Campo unit during the Jurassic indicates that, in a pre-rift section, both units were not as close as they are nowadays. The superposition likely occurred through the activity of the Jurassic ESZ that was interpreted as an extraction fault by Petri et al. (2019). In addition, the ESZ was active in greenschist facies conditions while being sub-horizontal and therefore it cannot correspond to a structure that exhumed efficiently rocks. This suggests that the exhumation of the Campo and Grosina units may have not occurred along the ESZ only, but was accomodated by other structures such as the Grosina detachment (Fig. 13ef), interpreted by Mohn et al. (2012) as a necking detachment. In this scenario, the ESZ is thus not directly responsible for the cooling of the Campo unit, leaving the effective age of the shear zone rather unconstrained. We can however postulate that it was active during the stretching and early necking phase (Fig. 13d) from late Triassic to early Jurassic, synchronous to the initiation of the rise of mantle and lower crust documented in the Lower Platta and Malenco units (Villa et al., 2000).

Observations in the distal domain (Err and Bernina units) indicate that deformation related to crustal necking was active between 190-175 Ma (Ribes et al., 2020), before being superseded by hyperextension in the distal domain from 175 Ma to 165 Ma. The cooling of the Campo unit is likely initiated around 180-175 Ma (position of node C3), which lies on the upper age limit of necking zones activity, and was achieved between 175-165 Ma. This end of cooling is coeval to the subsidence and the drowning of the necking zones documented in the post-Toarcian sediments

(Ribes et al., 2020). This implies that a complete heating-cooling cycle is recorded in the necking zone during its formation and that cooling of the necking zone may substantially postdate the main phase of necking but predates mantle exhumation that occurred at 165 Ma.

7. CONCLUSION

This contribution discussed the structural and thermal evolution of two basement units (i.e. Campo-Grosina units) in the Austroalpine nappes preserving the relics of the former necking zone of the Adriatic rifted margin. We report new $^{40}Ar/^{39}Ar$ ages from these two units that record a contrasted cooling history:

- $^{40}Ar/^{39}Ar$ ages from the Grosina unit lie at 261 ± 2 Ma for muscovite and at 246 ± 13 Ma and 245 ± 2 Ma for biotite.

- $^{40}Ar/^{39}Ar$ ages from the Campo unit are clearly younger, between 182 to 178 Ma for muscovite and between 174 and 171 Ma for biotite, with occasional older ages at 218 ± 2 Ma for muscovite and at 214 ± 3 Ma for biotite.

- In the Campo unit, 3 out of 4 dated amphiboles led to geologically meaningless dates, and the only interpretable $^{40}Ar/^{39}Ar$ interpretable age carries a large uncertainty with an inverse isochron age between 210 ± 4 Ma and 177 ± 13 Ma. These amphiboles suffered from both a low potassium content, and strong incorporation of extraneous argon caused by the intrusion of the Permian Sondalo gabbroic complex in the Campo unit.

The cooling history of the two units was modelled using a Monte Carlo approach based on DiffArgP, which allowed to constrain:

- a post-Variscan Permo-Triassic slow cooling history of 5-10 °C/Myr in the Grosina unit, that is characteristic of the conductive cooling of the continental lithosphere after an orogenic phase.

- a Jurassic rapid cooling of 25-100 °C/Myr in the Campo unit that is characteristic for tectonically-exhumed basement rocks. This exhumation was likely initiated at around 185 Ma, the

associated cooling being delayed by a few millions of years. A re-heating of the necking zone is suspected, but its characteristics remain to be better constrained.

ACKNOWLEDGMENTS

BP benefited from an excellence scholarship “Eole” from the French-Dutch network (RFN-FNA). Research was funded by an ExxonMobil grant to G. Manatschal. R. van Elsas and K. Kuiper are particularly thanked for mineral separation and preparation, respectively. M.-E. Epin and P. Wernert are gratefully thanked for their assistance during the sampling campaign. C. Warren is thanked for allowing us to use and adapt DiffArgP. We thank the two reviewers and the Editor N. Malaspina for their relevant comments and suggestions.

SUPPLEMENTARY MATERIAL

Supplementary Table S1: Representative mineral composition of dated samples

Supplementary Table S2: $^{40}Ar/^{39}Ar$ on muscovite geochronology data

Supplementary Table S3: $^{40}Ar/^{39}Ar$ on biotite geochronology data

Supplementary Table S4: $^{40}Ar/^{39}Ar$ on hornblende geochronology data

Supplementary Table S5: Compilation of pre-Alpine ages from the Campo and Grosina units

Supplementary Figure S6: Microphotographs of samples used for geochronology and mineral composition analyses

Supplementary Figure S7: Compilation of published and new ages for the Campo and Grosina units

Supplementary Text S8: DiffArgP modelling strategy

FIGURES

Sample name	Coordinates	Rock type	Assemblage	Mineral	Mineral chemistry			Core			Rim			Total			40Ar/39Ar dates	
					Amp Altot Bt Xmg Ms Si	Amp NaM4 Ms Pg	Amp Ti Bt Ti Ms Ti	T (°C)	P (kbar)	n	T (°C)	P (kbar)	n	T (°C)	P (kbar)	n	Ma	± 2σ
Grosina unit																		
GM119	46.39640°N 10.23004°E	Granodiorite	Bt-Pl-Kfs-Qtz-Ilm	Biotite	0.37-0.43	0.08-0.21		681 ± 16	/	10	617 ± 50	/	10	649 ± 49	/	20	246 ± 13 Ma	
GM264	46.34994°N 10.17277°E	Grt-paragneiss	Bt-Ms-Grt-Pl-Kfs-Qtz-Ilm	Biotite Muscovite	0.5 > 3.1	< 0.10 0.09-0.15	 < 0.03	569 ± 6 578 ± 20	/ /	10 10	572 ± 9 561 ± 33	/ /	10 10	570 ± 8 569 ± 28	/ /	20 20	245 ± 2 Ma 261 ± 2 Ma	
Campo unit																		
CP003b	46.35977°N 10.33070°E	Migmatitic micashist	Ms-Bt-Grt-Sil-Pl-Kfs-Qtz-Ilm	Muscovite	3.02	0.13	0.04-0.07	693 ± 37	/	10	689 ± 30	/	10	691 ± 33	/	20	218 ± 2 Ma	
CP010g	46.36312°N 10.24878°E	Amphibolite	Hbl-Pl-Ilm	Amphibole	1.99	0.14	0.07	/	/	/	/	/	/	/	/	/	Ex ^{40}Ar	
CP028c	46.33248°N 10.31080°E	Bt-Ms micaschist	Bt-Ms-Pl-Qtz-Ilm	Biotite Muscovite	0.46 3.00	0.2 0.7	 0.05	696 ± 16 696 ± 5	/ /	10 10	699 ± 17 694 ± 11	/ /	10 10	698 ± 16 695 ± 8	/ /	20 20	174 ± 2 Ma 178 ± 5 Ma	
CP031a	46.33479°N 10.31815°E	Grt-granodiorite	Bt-Hbl-Grt-Pl-Qtz-Ilm	Amphibole Biotite	2.29-2.67 0.44	0.16-0.19 0.07-0.14	0.05-0.09	/ 585 ± 36	8 ± 1 /	10 10	/ 576 ± 45	10 ± 1 /	10 10	/ 581 ± 40	9 ± 1 /	20 20	210-177 ± 4-13 Ma 173 ± 2 Ma	
CP032c	46.35123°N 10.35480°E	Amp-gabbro	Hbl-Cpx-Opx-Pl-Mag	Amphibole	2.29	0.25	0.34	950 ± 20	6 ± 2	10	940 ± 30	6 ± 3	9	940 ± 30	6 ± 2	19	Ex ^{40}Ar	
CP034c	46.34941°N 10.36257°E	Grt-granodiorite	Bt-Grt-Pl-Ilm	Biotite	0.60-0.62	0.07-0.08		563 ± 10	/	10	563 ± 9	/	10	563 ± 10	/	20	214 ± 3 Ma	
CM234	46.33479°N 10.31815°E	Amphibolite	Amp-Pl-Ilm	Amphibole	2.3	0.1	0.08	/	/	/	/	/	/	/	/	/	Ex ^{40}Ar	
CM260	46.35939°N 10.25048°E	Grt-micaschist	Bt-Ms-Grt-Pl-Kfs-Qtz-Ilm	Biotite Muscovite	0.4 3.04	0.12 0.14-0.16	 0.03	611 ± 17 572 ± 32	/ /	10 10	611 ± 11 562 ± 44	/ /	10 10	611 ± 14 567 ± 38	/ /	20 20	171 ± 1 Ma 182 ± 2 Ma	

Table 1: Sample list, coordinates, rock type, mineral assemblage and composition with average values of thermobarometric estimates, and ^{40}Ar/^{39}Ar dates. See text for details and Supplementary Material S1 for detailed mineral composition and thermobarometric estimates.

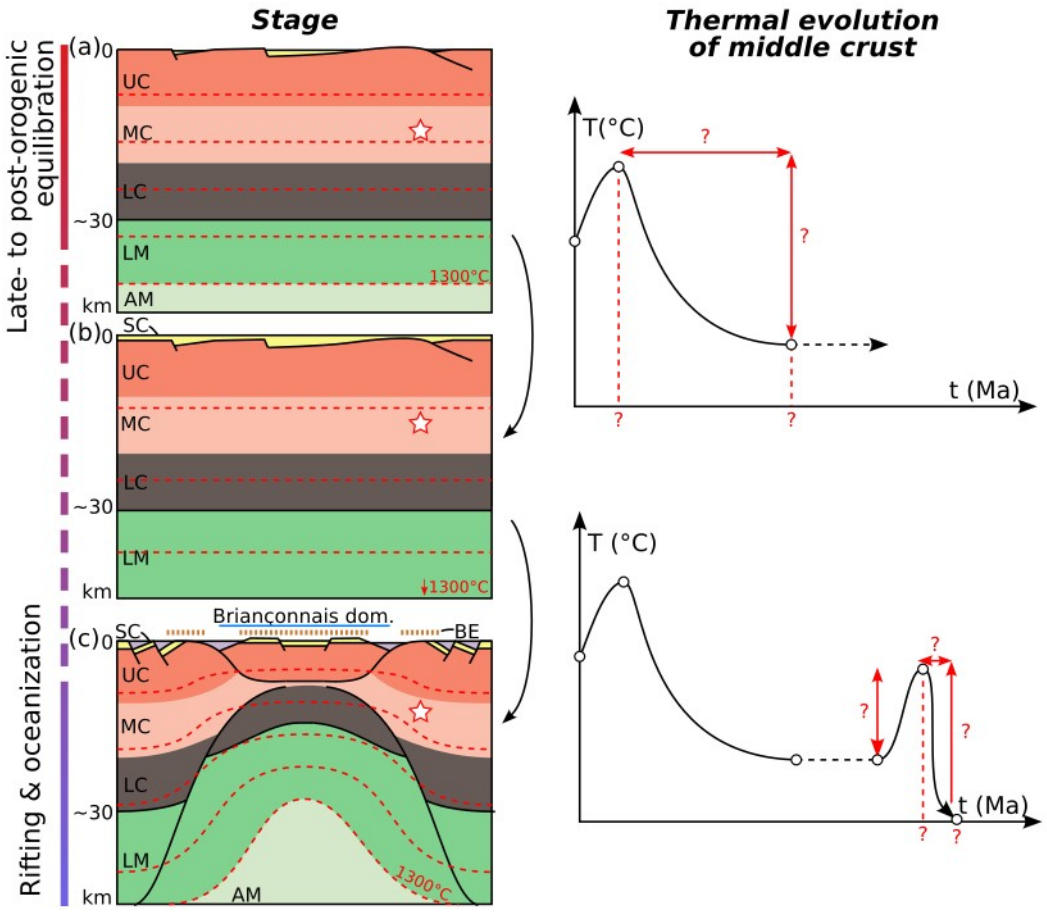

866

867 **Fig. 1:** Schematic thermal evolution of the continental lithosphere in the middle crust of a
868 future necking zone from (a) a post-orogenic stage characterized by active extension (high angle
869 normal faults and detachment faults), (b) a conductive lithospheric cooling, and (c) subsequent
870 rifting and crustal necking. Sedimentary basins and thermal evolution not to scale. BE: basement
871 exposure/erosion; SC: sedimentary cover; UC: upper crust; MC: middle crust; LC: lower crust; LM:
872 lithospheric mantle; AM: asthenospheric mantle.

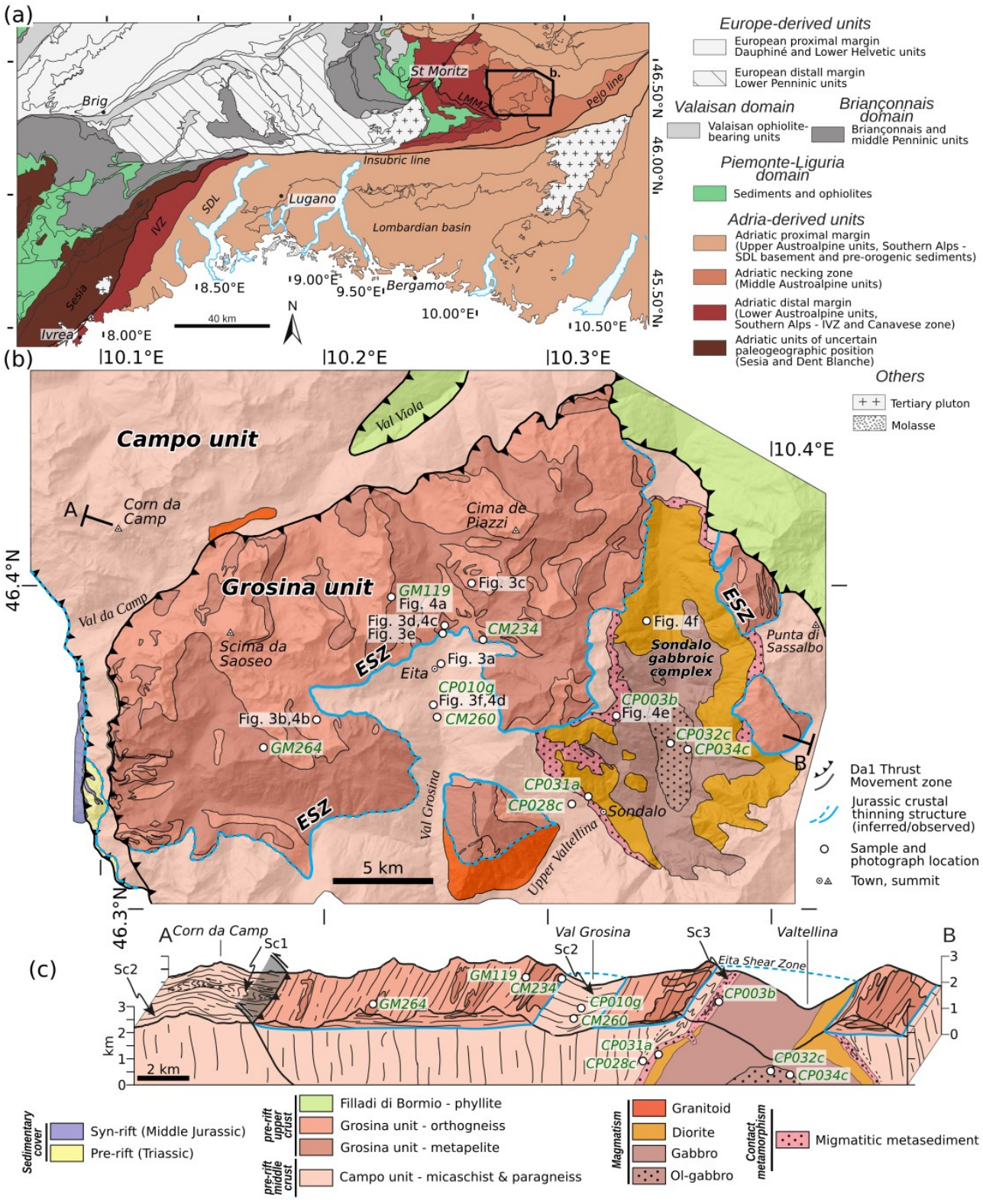

873

874 **Fig. 2:** (a) Tectonic map of the central part of the Alps reporting the paleogeographic origin
875 of the different units, modified from Petri et al. (2019). IVZ: Ivrea-Verbano Zone; SDL: Serie dei
876 Laghi; LMMZ: Lunghin-Mortirolo Movement Zone. (b) Geological map of the study area modified
877 from Mohn et al. (2011), the 1:10,000 and 1:25,000 geological maps of Italy and personal

878 observations, and (c) schematic cross-section. Location of samples used for geochronology is
879 reported in green on the map and located or projected on the cross-section; location of photographs
880 is reported in black.

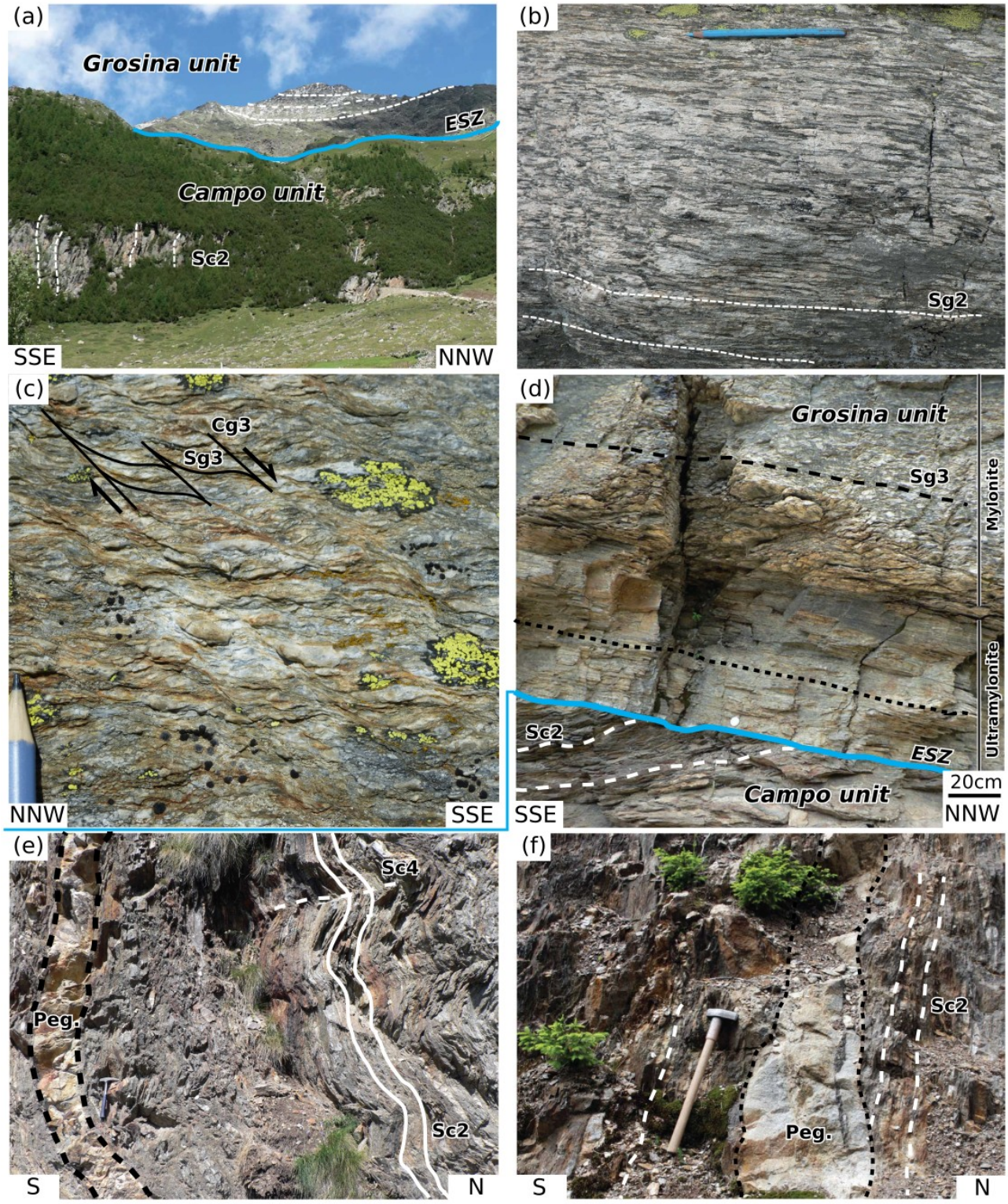

881

Fig. 3: Field photographs. (a) Panoramic view of the Campo/Grosina units close to the Eita village. Note the vertical Sc2 foliation of the Campo unit and the horizontal foliation of the Grosina unit. Grosina unit: (b) Mylonitic orthogneiss showing the sub-horizontal amphibolite-facies Sg2 foliation; (c) greenschist facies S-C structures associated to the Sg3 foliation. (d) Contact between the Campo metasediments with tilted Sc2 foliation and the Grosina orthogneiss with Sg3 greenschist facies fabric along the ESZ. Campo unit: (e) Micaschist and pegmatitic dykes presenting Fc4 folds; (f) pegmatitic dyke cross-cutting the Sc2 planar fabric of metasediments.

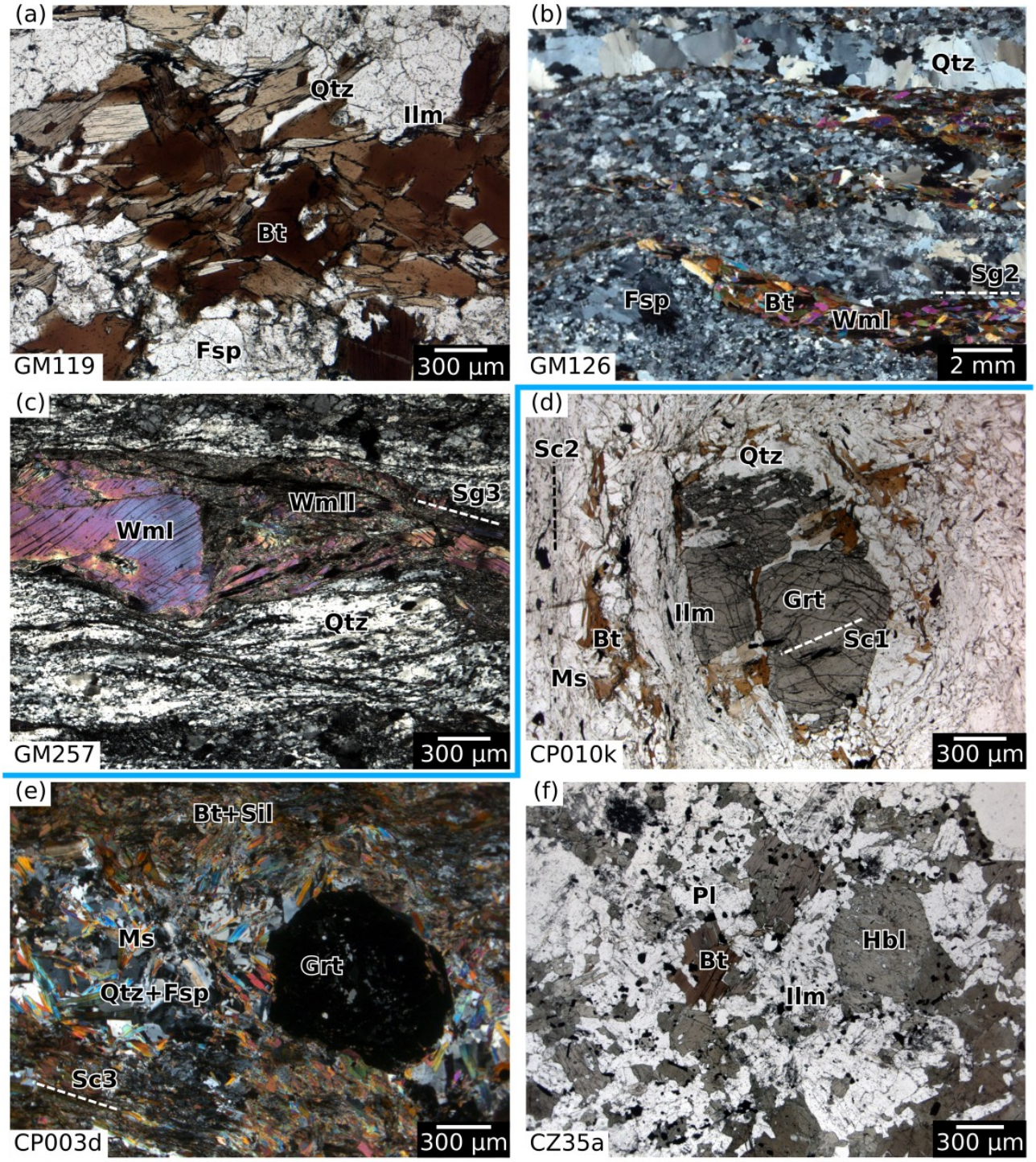

Fig. 4: Photomicrographs illustrating various lithologies for (a-c) the Grosina unit and (d-f) the Campo unit. (a) Undeformed granodiorite with preserved magmatic biotites. (b) Amphibolite-facies mylonitic orthogneiss with metamorphic biotite and white mica I. Note the quartz recrystallization through grain-boundary migration. (c) Greenschist facies recrystallization of porphyroclastic white mica I into white mica II. (d) Garnet-bearing micaschist with metamorphic

biotite and muscovite aligned along the Sc2 foliation. (e) Garnet–sillimanite–biotite migmatite in the contact aureole of the Sondalo gabbro, with post-peak crystallization of muscovite in quartz–feldspar-garnet leucocratic layer. (f) Magmatic hornblende and biotite from a diorite from the Sondalo pluton.

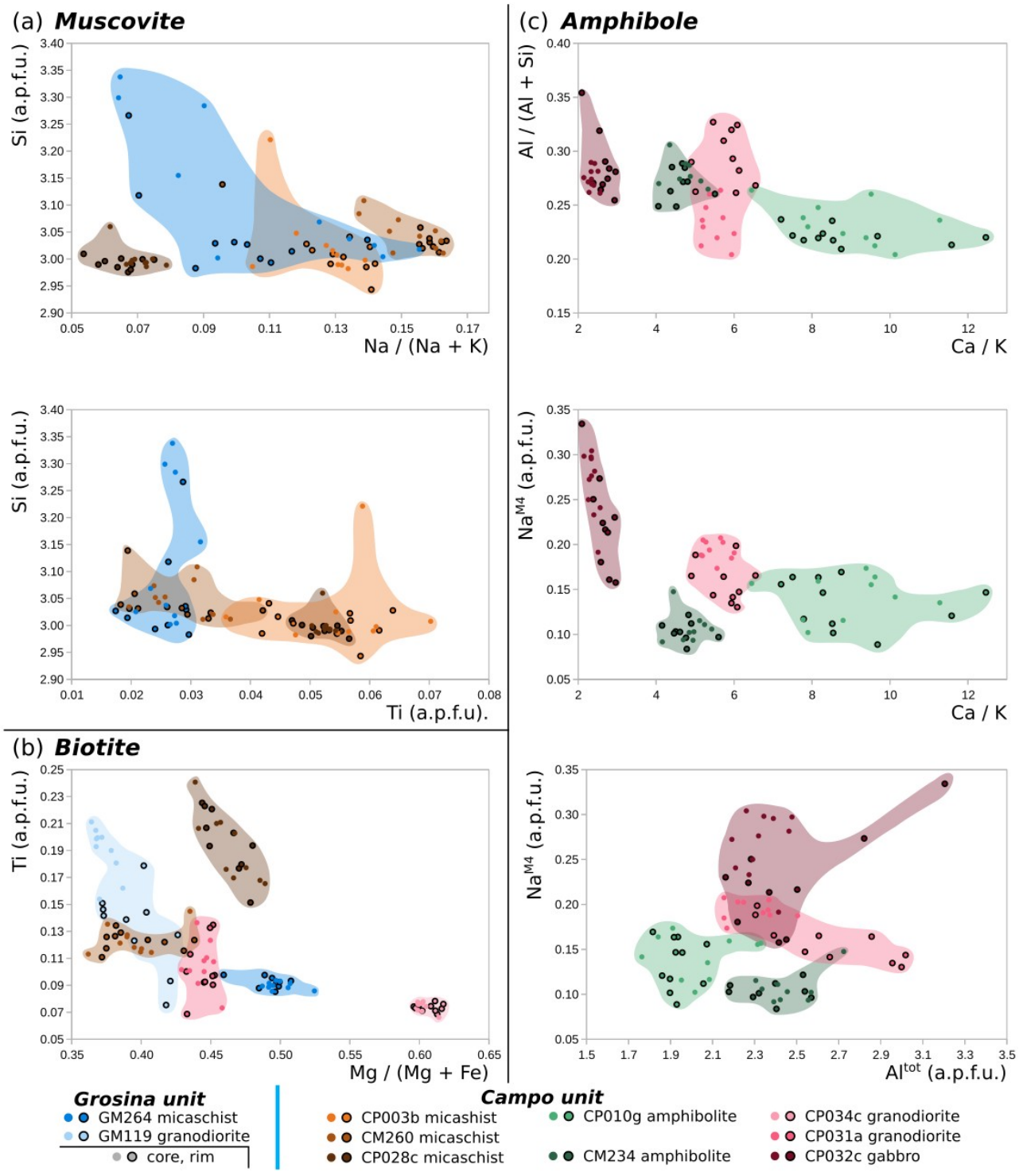

Fig. 5: Mineral composition plots for (a) muscovite, (b) biotite and (c) amphibole.

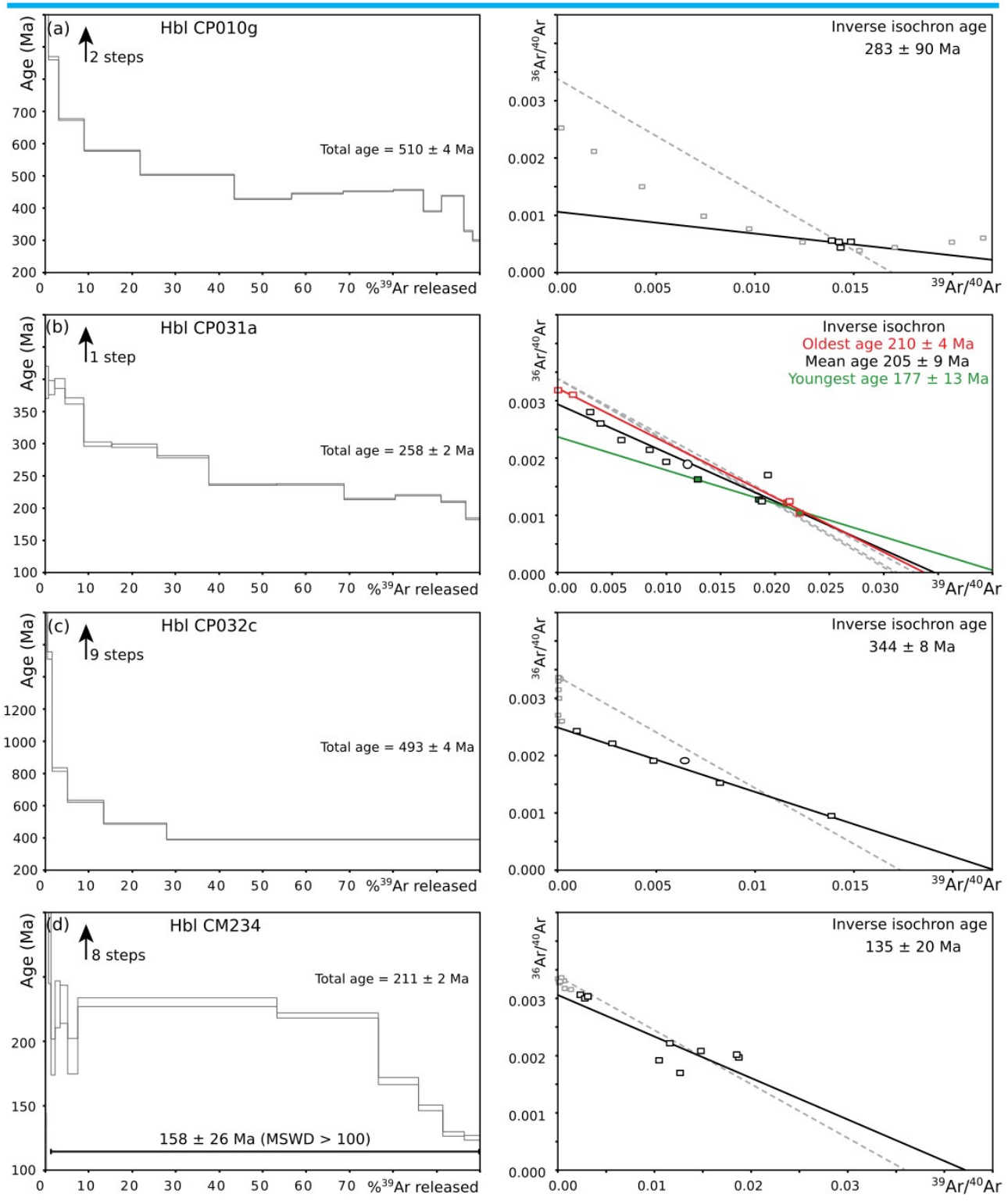

Fig. 6: ^{40}Ar–^{39}Ar step-release spectra and inverse isochron plots for hornblende from the Campo unit. Steps used to determine the "plateau" ages (if possible) are indicated by the horizontal black lines. Ages in bold and blue indicate the most reliable age between "plateau" age, total fusion age and inverse isochron age. Sample locations are shown in Fig. 2. Analysed mineral, sample and

experiment (in brackets) name are indicated (top side) along with the mean square weighted deviation (MSWD) of the "plateau" age and the total fusion age (bottom right-hand side).

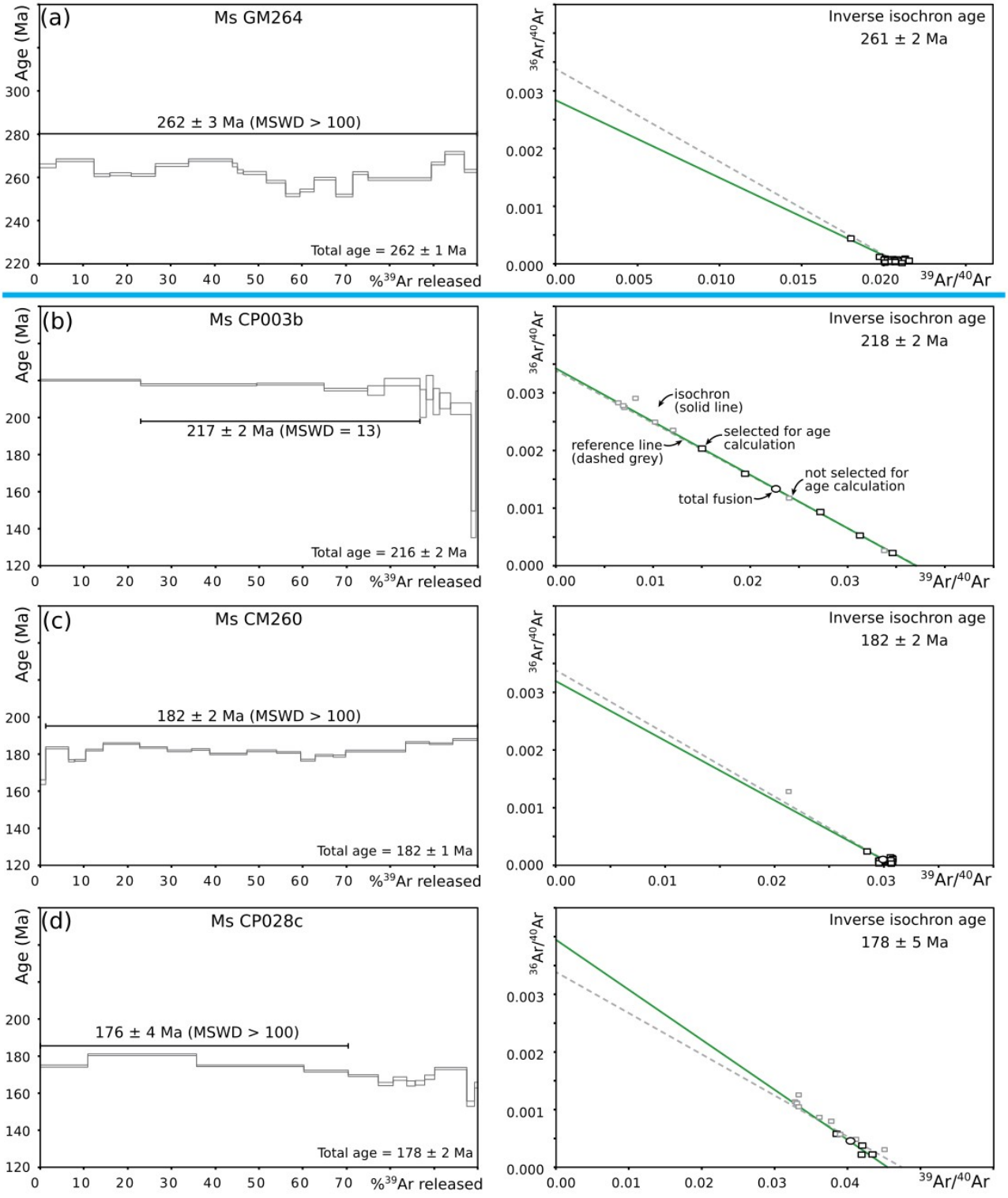

Fig. 7: ^{40}Ar–^{39}Ar step-release spectra and inverse isochron plots for muscovite from (a) the Grosina unit and (b-d) the Campo unit. Steps used to determine the "plateau" ages (if possible) are

911 indicated by the horizontal black lines. Ages in bold and blue indicate the most reliable age between
912 “plateau” age, total fusion age and inverse isochron age. Sample locations are shown in Fig. 2.
913 Analysed mineral, sample and experiment (in brackets) name are indicated (top side) along with the
914 mean square weighted deviation (MSWD) of the “plateau” age and the total fusion age (bottom
915 right-hand side).

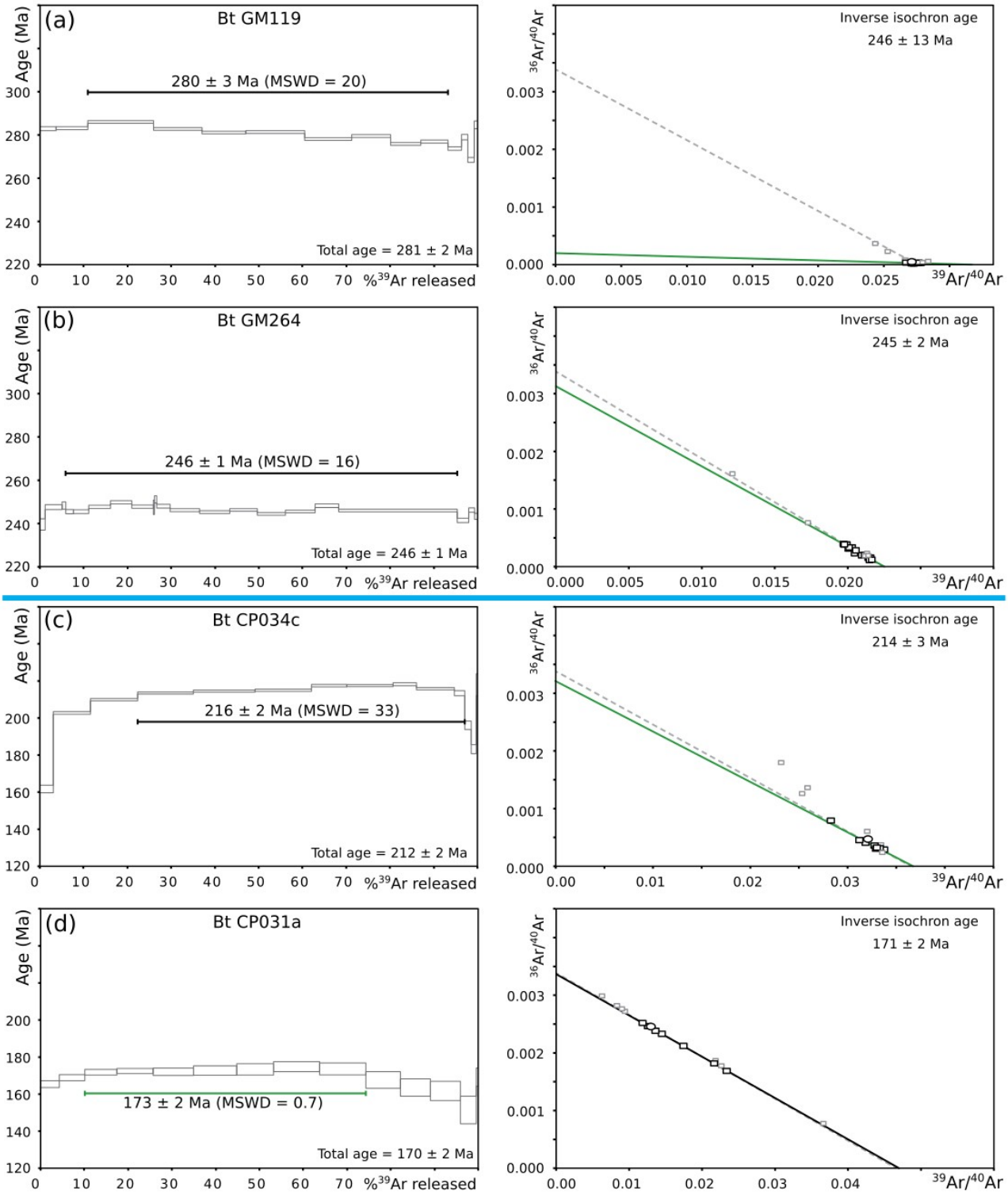

Fig. 8: ^{40}Ar–^{39}Ar step-release spectra and inverse isochron plots for biotite from (a,b) the Grosina unit and (c,d) the Campo unit. Steps used to determine the "plateau" ages (if possible) are indicated by the horizontal black lines. Ages in bold and blue indicate the most reliable age between "plateau" age, total fusion age and inverse isochron age. Sample locations are shown in Fig. 2.

Analysed mineral, sample and experiment (in brackets) name are indicated (top side) along with the mean square weighted deviation (MSWD) of the “plateau” age and the total fusion age (bottom right-hand side).

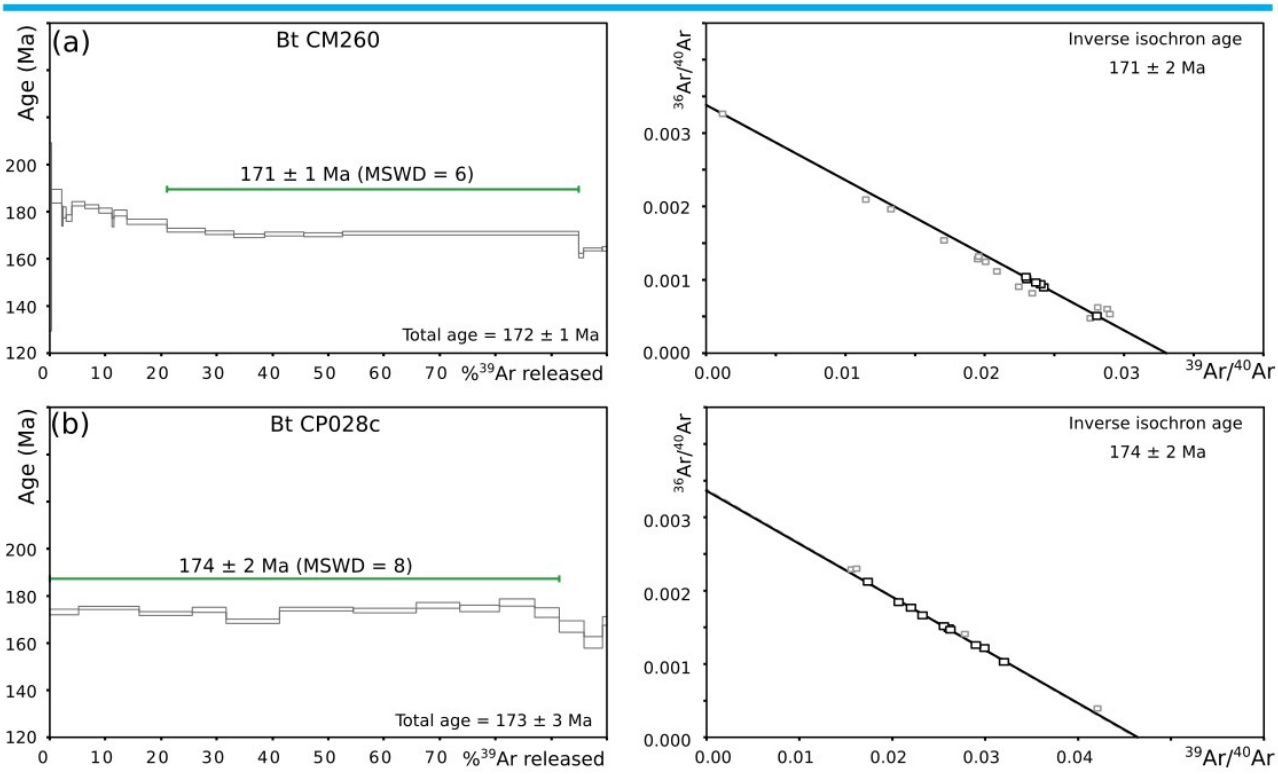

Fig. 9: ^{40}Ar–^{39}Ar step-release spectra and inverse isochron plots for biotite from the Campo unit. Steps used to determine the “plateau” ages (if possible) are indicated by the horizontal black lines. Ages in bold and blue indicate the most reliable age between “plateau” age, total fusion age and inverse isochron age. Sample locations are shown in Fig. 2. Analysed mineral, sample and experiment (in brackets) name are indicated (top side) along with the mean square weighted deviation (MSWD) of the “plateau” age and the total fusion age (bottom right-hand side).

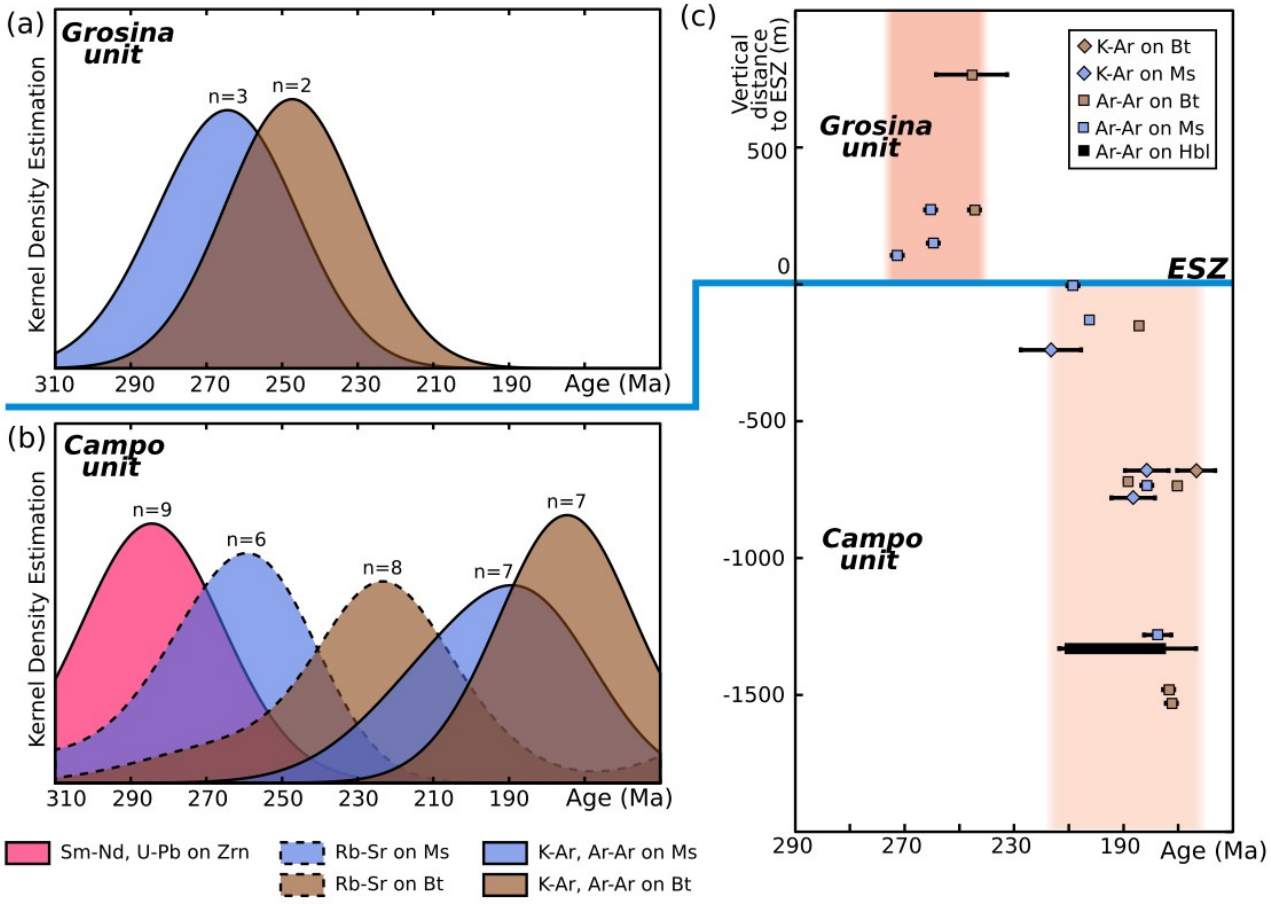

931

932 **Fig. 10:** Kernel Density Estimates (KDE) histogram of (a) the Grosina unit, (b) the Campo
933 unit and (c) age vs. vertical distance to the ESZ (one data point per sample). Plots were made using
934 data from this study and data from the literature. See text for details; complete dataset provided as
935 Supplementary Material S5. Errors are represented at a 2σ level of confidence; KDE plots were
936 produced using IsoplotR (Vermeesch, 2018).

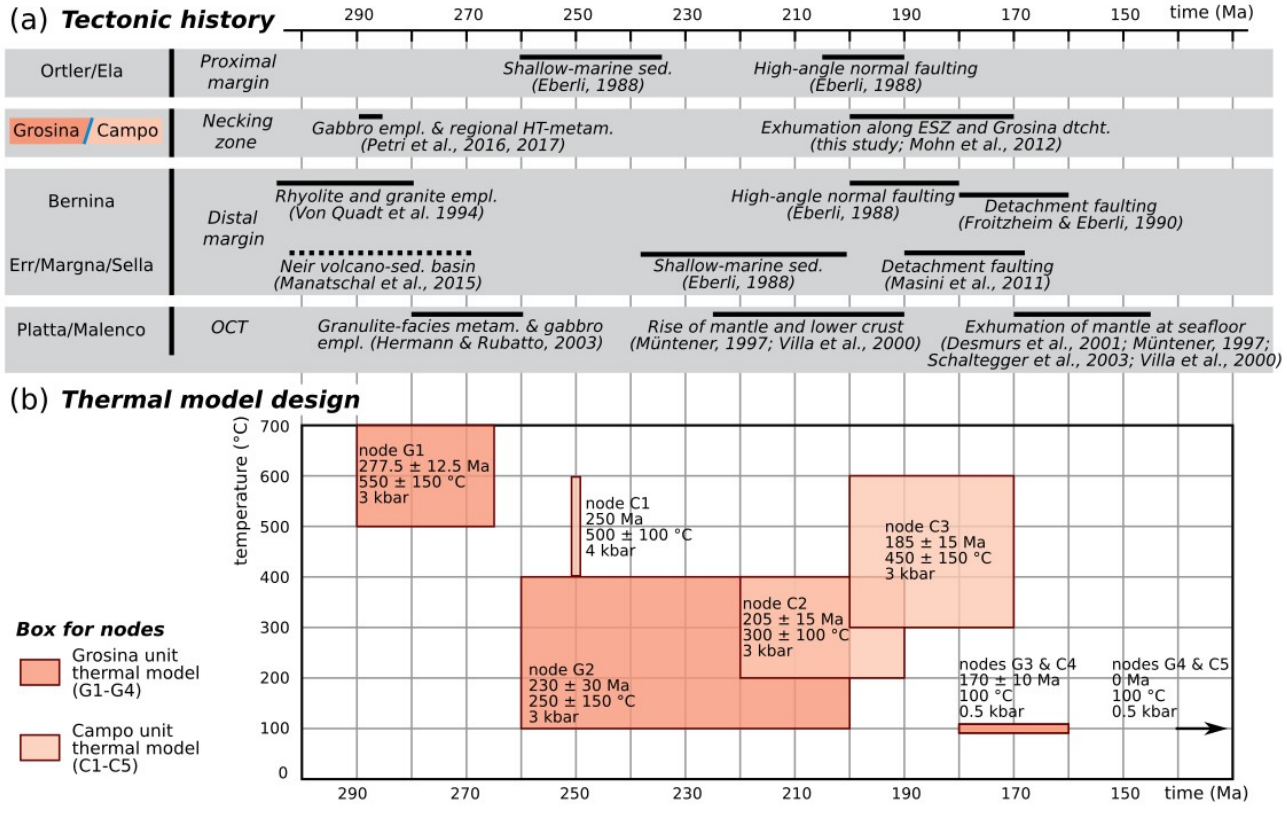

Fig. 11: (a) Compilation of tectonic, magmatic and metamorphic phases in the Austroalpine nappes (Eastern Alps) used to construct (b) the thermal models that served as input for DiffArgP-based Monte Carlo simulations. Thermal models for the Grosina unit are defined by nodes G1 to G4; thermal models for the Campo unit are defined by nodes C1 to C5.

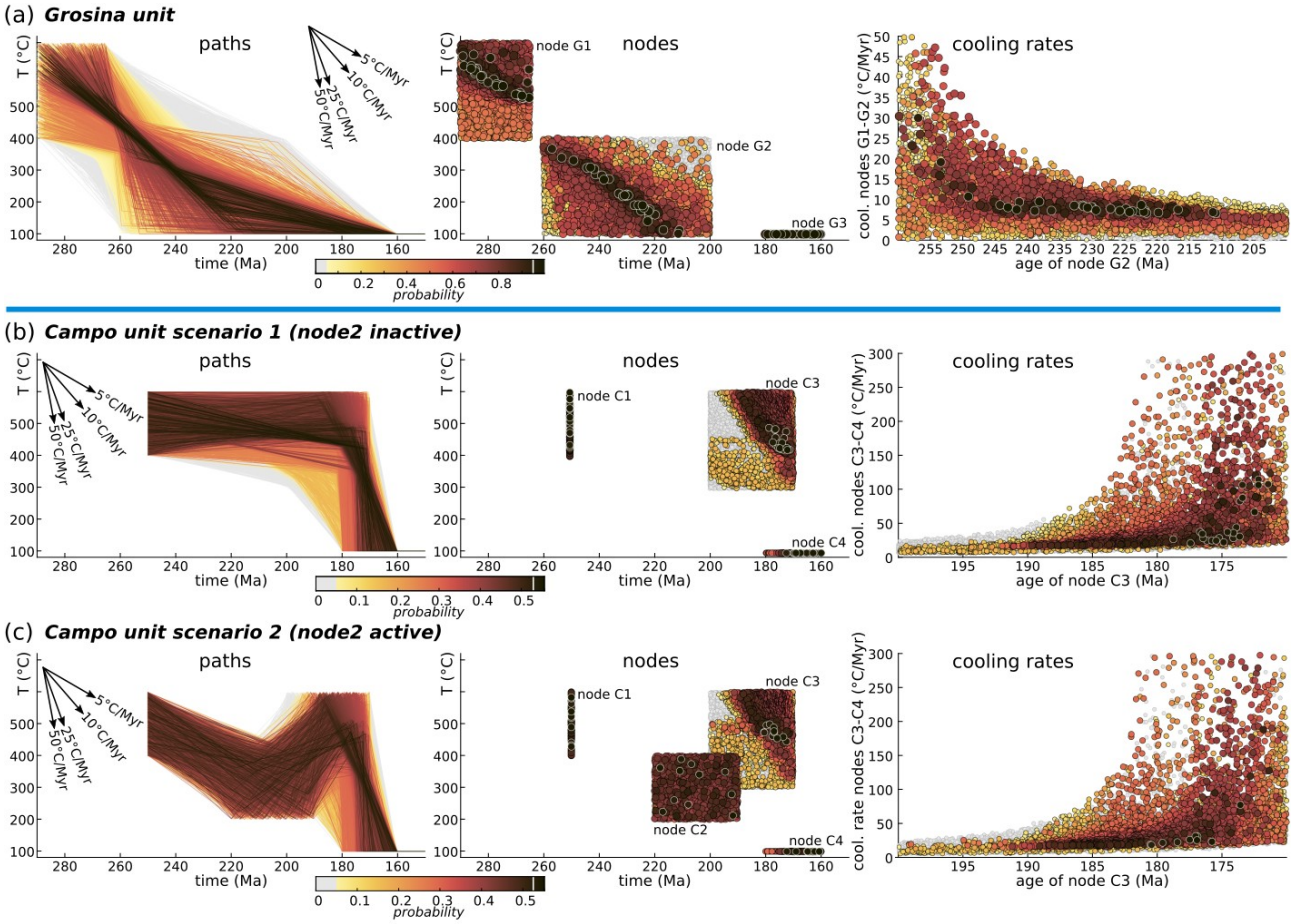

Fig. 12: Paths, nodes and cooling rates of key nodes of DiffArgP-based Monte Carlo simulations for the thermal scenario of (a) the Grosina unit, (b) the Campo unit with node C2 inactive involving a 2-phase cooling (slow pre-rift and early-rift, fast syn-rift) or (c) the Campo unit with node C2 active, forcing the pre-rift cooling to be interrupted by an Early Jurassic re-heating (between nodes C2 and C3). Each scenario was explored by 10,000 random paths which nodes characteristics (position and associated degree of freedom) are specified in Fig. 11. Paths with $p < 0.05$ are discarded and grey-coloured, nodes from paths within the 5 highest probability % are circled in white. Path colour as well as nodes colour and size depend on the goodness of the temperature-time path to fit measured Ar-Ar ages from our study. See text for details.

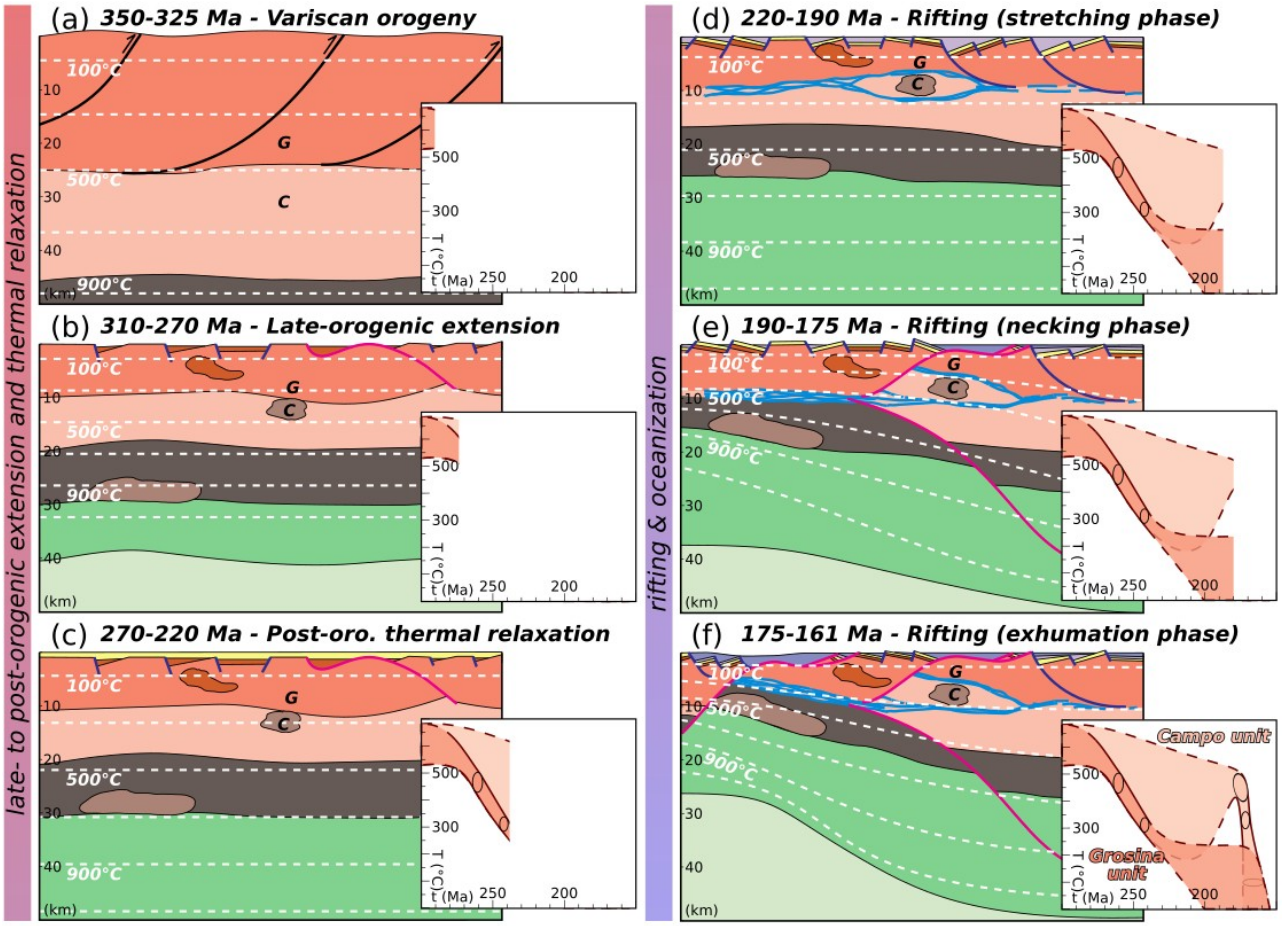

Fig. 13: Synthetic tectonic and thermal evolution of the Austroalpine nappes and notably the Campo (light pink) and Grosina (darker pink) units, encompassing (a) the Variscan orogeny, (b) late-orogenic collapse and extension during which the continental crust returns to a standard equilibrated thickness (30-40 km), followed by (c) a period of thermal relaxation from Middle Permian to late Triassic, until a new tectonic cycle develops with the opening of the Alpine Tethys separated in three phases: (d) the stretching of the continental crust by high-angle normal faults and extraction faults, (e) the necking of the continental crust with the concomitant activity of extraction faults (see Petri et al., 2019 for details) and necking detachment faults and (f) exhumation of deep continental crust and lithospheric mantle through multiple detachment faults. Modified from Mohn et al. (2012) and Petri et al. (2019, 2017, 2016). Thermal evolution of the Campo (C) and Grosina (G) units are constrained using the location of nodes and paths with the highest probabilities reported in Fig. 12.

References

Beltrando, M., Stockli, D.F., Decarlis, A., Manatschal, G., 2015. A crustal-scale view at rift localization along the fossil Adriatic margin of the Alpine Tethys preserved in NW Italy. Tectonics 34, 1927–1951. https://doi.org/10.1002/2015TC003973

Beltrando, M., Zibra, I., Montanini, A., Tribuzio, R., 2013. Crustal thinning and exhumation along a fossil magma-poor distal margin preserved in Corsica: A hot rift to drift transition? Lithos 168–169, 99–112. https://doi.org/10.1016/j.lithos.2013.01.017

Bergomi, M.A., Boriani, A., 2012. Late Neoproterozoic - Early Paleozoic accretion of the Southalpine and Austroalpine basements of Central Alps (Italy). Géologie Fr. 1, 69.

Bertotti, G., 1991. Early Mesozoic extension and Alpine shortening in the western Southern Alps: The geology of the area between Lugano and Menaggio (Lombardy, northern Italy). Mem. Sci. Geol. 43, 17–123.

Bertotti, G., Seward, D., Wijbrans, J., ter Voorde, M., Hurford, A.J., 1999. Crustal thermal regime prior to, during, and after rifting: A geochronological and modeling study of the Mesozoic South Alpine rifted margin. Tectonics 18, 185–200. https://doi.org/10.1029/1998tc900028

Bianchi Potenza, B., Carimati, R., Potenza, R., Testa, B., 1985. Considerazioni cronologiche sul filone trachitico di Sondalo (Lombardia, Valtellina). Atti Della Soc. Sci. Nat. E Mus. Civ. Storia Nat. Milano 120, 141–144.

Boriani, A., Bergomi, M., Giobbi, E., 2005. Relationships between late-Variscan strike-slip faults and the emplacement of intrusive magmas in the South Alpine and in the Upper-Austroalpine basement of Central Alps. Geophys. Res. Abstr. 7, 11051.

Boriani, A., Bini, A., Berra, F., 2011. Note illustrative della Carta Geologica d'Italia alla scala 1:50.000, Foglio 56 Sondrio. Serv. Geol. Ital. ISPRA 242 p.

Braga, R., Giacomini, F., Messiga, B., Tribuzio, R., 2001. The Sondalo Gabbroic Complex (Central Alps, Northern Italy): Evidence for Emplacement of Mantle-Derived Melts into Amphibolite Facies Metapelites. Phys. Chem. Earth Part Solid Earth Geod. 26, 333–342. http://doi.org/10.1016/S1464-1895(01)00063-1

Burg, J.-P., Van Den Drissche, J., Brun, J.-P., 1994. Syn- to post-thickening extension in the Variscan Belt of Western Europe: Modes and structural consequences. Géologie Fr. 3, 33–51.

Busch, J.P., van der Pluijm, B.A., Hall, C.M., Essen, E.J., 1996. Listric normal faulting during postorogenic extension revealed by 40Ar/39Ar thermochronology near the Robertson Lake shear zone, Grenvill orogen, Canada. Tectonics 15, 387–402. http://doi.org/10.1029/95TC03501

Chenin, P., Manatschal, G., Decarlis, A., Schmalholz, S.M., Duretz, T., Beltrando, M., 2019. Emersion of Distal Domains in Advanced Stages of Continental Rifting Explained by Asynchronous Crust and Mantle Necking. Geochem. Geophys. Geosystems 20, 3821–3840. https://doi.org/10.1029/2019GC008357

Chenin, P., Schmalholz, S.M., Manatschal, G., Duretz, T., 2020. Impact of crust–mantle mechanical coupling on the topographic and thermal evolutions during the necking phase of 'magma-poor' and 'sediment-starved' rift systems: A numerical modeling study. Tectonophysics 786, 228472–228472. https://doi.org/10.1016/j.tecto.2020.228472

de Jong, K., Féraud, G., Ruffet, G., Amouric, M., Wijbrans, J.R., 2001. Excess argon incorporation in phengite of the Mulhacén Complex: submicroscopic illitization and fluid ingress during

late Miocene extension in the Betic Zone, south-eastern Spain. Chem. Geol. 178, 159–195. https://doi.org/10.1016/S0009-2541(00)00411-3

Decarlis, A., Beltrando, M., Manatschal, G., Ferrando, S., Carosi, R., 2017. Architecture of the Distal Piedmont-Ligurian Rifted Margin in NW Italy: Hints for a Flip of the Rift System Polarity. Tectonics 36, 2388–2406. https://doi.org/10.1002/2017TC004561

Decarlis, A., Dallagiovanna, G., Lualdi, A., Maino, M., Seno, S., 2013. Stratigraphic evolution in the Ligurian Alps between Variscan heritages and the Alpine Tethys opening: A review. Earth-Sci. Rev. 125, 43–68. http://doi.org/10.1016/j.earscirev.2013.07.001

Del Moro, A., Notarpietro, A., 1987. Rb-Sr Geochemistry of some Hercynian granitoids overprinted by eo-Alpine metamorphism in the Upper Valtellina, Central Alps. Schweiz. Mineral. Petrogr. Mitteilungen 67, 295–306.

Eberli, G.P., 1988. The evolution of the southern continental margin of the Jurassic Tethys Ocean as recorded in the Allgäu Formation of the Austroalpine Nappes of Graubünden (Switzerland). Eclogae Geol. Helvetiae 81, 175–214.

Ernst, W.G., Liu, J., 1998. Experimental phase-equilibrium study of Al- and Ti-contents of calcic amphibole in MORB; a semiquantitative thermobarometer. Am. Mineral. 83, 952–969. https://doi.org/10.2138/am-1998-9-1004

Esedo, R., van Wijk, J., Coblentz, D., Meyer, R., 2012. Uplift prior to continental breakup: Indication for removal of mantle lithosphere? Geosphere 8, 1078–1085. https://doi.org/10.1130/GES00748.1

Ewing, T.A., Rubatto, D., Beltrando, M., Hermann, J., 2015. Constraints on the thermal evolution of the Adriatic margin during Jurassic continental break-up: U–Pb dating of rutile from the Ivrea–Verbano Zone, Italy. Contrib. Mineral. Petrol. 169, 44. https://doi.org/10.1007/s00410-015-1135-6

Foland, K.A., 1983. 40Ar/39Ar incremental heating plateaus for biotites with excess argon. Chem. Geol. 41, 3–21. http://dx.doi.org/10.1016/S0009-2541(83)80002-3

Froitzheim, N., Eberli, G.P., 1990. Extensional detachment faulting in the evolution of a Tethys passive continental margin, Eastern Alps, Switzerland. Geol. Soc. Am. Bull. 102, 1297–1308. https://doi.org/10.1130/0016-7606(1990)102<1297:edfite>2.3.co;2

Froitzheim, N., Schmid, S.M., Conti, P., 1994. Repeated change from crustal shortening to orogen-parallel extension in the Austroalpine units of Graubünden. Eclogae Geol. Helvetiae 87, 559–612.

Froitzheim, N., Schmid, S.M., Frey, M., 1996. Mesozoic paleogeography and the timing of eclogite-facies metamorphism in the Alps: A working hypothesis. Eclogae Geol. Helvetiae 89, 81–110.

Galli, A., Grassi, D., Sartori, G., Gianola, O., Burg, J.-P., Schmidt, M.W., 2019. Jurassic carbonatite and alkaline magmatism in the Ivrea zone (European Alps) related to the breakup of Pangea. Geology 47, 199–202. https://doi.org/10.1130/G45678.1

Grove, M., Harrison, T.M., 1996. 40 Ar (super *) diffusion in Fe-rich biotite. Am. Mineral. 81, 940–951. https://doi.org/10.2138/am-1996-7-816

Handy, M.R., Herweg, M., Kamber, B.S., Tietz, R., Villa, I.M., 1996. Geochronologic, petrologic and kinematic constraints on the evolution of the Err-Platta boundary, part of a fossil continent-ocean suture in the Alps (eastern Switzerland). Schweiz. Mineral. Petrogr. Mitteilungen 76, 453–474.

Hansmann, W., Müntener, O., Hermann, J., 2001. U-Pb zircon geochronology of a tholeiitic intrusion and associated migmatites at a continental crust-mantle transition, Val Malenco, Italy. Schweiz. Mineral. Petrogr. Mitteilungen 81, 239–255.

Hanson, G.N., El Tahlawi, M.R., Weber, W., 1966. K-Ar and Rb-Sr ages of pegmatites in the South Central Alps. Earth Planet. Sci. Lett. 1, 407–413. http://doi.org/10.1016/0012-821X(66)90037-9

Harrison, T.M., Célérier, J., Aikman, A.B., Hermann, J., Heizler, M.T., 2009. Diffusion of 40Ar in muscovite. Geochim. Cosmochim. Acta 73, 1039–1051. https://doi.org/10.1016/j.gca.2008.09.038

Harrison, T.M., Duncan, I., McDougall, I., 1985. Diffusion of 40Ar in biotite: Temperature, pressure and compositional effects. Geochim. Cosmochim. Acta 49, 2461–2468. https://doi.org/10.1016/0016-7037(85)90246-7

Henry, D.J., 2005. The Ti-saturation surface for low-to-medium pressure metapelitic biotites: Implications for geothermometry and Ti-substitution mechanisms. Am. Mineral. 90, 316–328. https://doi.org/10.2138/am.2005.1498

Hermann, J., Müntener, O., 1992. Strukturelle Entwicklung im Grenzbereich zwischen dem penninischen Malenco-Ultramafitit ind dem Unterostalpin (Magna- und Sella-Decke). Schweiz. Mineral. Petrogr. Mitteilungen 72, 225–240.

Hermann, J., Müntener, O., Günther, D., 2001. Differentiation of Mafic Magma in a Continental Crust-to-Mantle Transition Zone. J. Petrol. 42, 189–206. https://doi.org/10.1093/petrology/42.1.189

Hermann, J., Müntener, O., Trommsdorff, V., Hansmann, W., Piccardo, G.B., 1997. Fossil crust-to-mantle transition, Val Malenco (Italian Alps). J. Geophys. Res. Solid Earth 102, 20123–20132. https://doi.org/10.1029/97jb01510

Hermann, J., Rubatto, D., 2003. Relating zircon and monazite domains to garnet growth zones: age and duration of granulite facies metamorphism in the Val Malenco lower crust. J. Metamorph. Geol. 21, 833–852. https://doi.org/10.1046/j.1525-1314.2003.00484.x

Hyodo, H., York, D., 1993. The discovery and significance of a fossilized radiogenic argon wave (argonami) in the Earth's crust. Geophys. Res. Lett. 20, 61–64. http://doi.org/10.1029/92GL02675

Kelley, S., 2002. Excess argon in K-Ar and Ar-Ar geochronology. Chem. Geol. 188, 1–22. http://doi.org/10.1016/S0009-2541(02)00064-5

Koppers, A.A.P., 2002. ArArCALC-software for 40Ar/39Ar age calculations. Comput. Geosci. 28, 605–619. https://doi.org/10.1016/s0098-3004(01)00095-4

Kuiper, K.F., Deino, A., Hilgen, F.J., Krijgsman, W., Renne, P.R., Wijbrans, J.R., 2008. Synchronizing Rock Clocks of Earth History. Science 320, 500–504. https://doi.org/10.1126/science.1154339

Lee, J.-Y., Marti, K., Severinghaus, J.P., Kawamura, K., Yoo, H.-S., Lee, J.B., Kim, J.S., 2006. A redetermination of the isotopic abundances of atmospheric Ar. Geochim. Cosmochim. Acta 70, 4507–4512. http://doi.org/10.1016/j.gca.2006.06.1563

Lo, C.-H., Onstott, T.C., 1989. 39Ar recoil artifacts in chloritized biotite. Geochim. Cosmochim. Acta 53, 2697–2711. http://dx.doi.org/10.1016/0016-7037(89)90141-5

McKenzie, D., 1978. Some remarks on the development of sedimentary basins. Earth Planet. Sci. Lett. 40, 25–32. https://doi.org/10.1016/0012-821X(78)90071-7

Meier, A., 2003. The Periadriatic Fault System in Valtellina (N-Italy) and the Evolution of the Southwestern Segment of the Eastern Alps. PhD Thesis, ETH Zurich.

Mohn, G., Manatschal, G., Beltrando, M., Masini, E., Kusznir, N., 2012. Necking of continental crust in magma-poor rifted margins: Evidence from the fossil Alpine Tethys margins. Tectonics 31. https://doi.org/10.1029/2011TC002961

Mohn, G., Manatschal, G., Masini, E., Müntener, O., 2011. Rift-related inheritance in orogens: a case study from the Austroalpine nappes in Central Alps (SE-Switzerland and N-Italy). Int. J. Earth Sci. 100, 937–961. https://doi.org/10.1007/s00531-010-0630-2

Mohn, G., Manatschal, G., Müntener, O., Beltrando, M., Masini, E., 2010. Unravelling the interaction between tectonic and sedimentary processes during lithospheric thinning in the Alpine Tethys margins. Int. J. Earth Sci. 99, 75–101. https://doi.org/10.1007/s00531-010-0566-6

Mohn, G., Tugend, J., Petri, B., McCarthy, A., Frizon de Lamotte, D., 2022. How to identify and study remnants of rifted margins in orogens?, in: Peron-Pinvidic, G. (Ed.), Continental Rifted Margins 1. https://doi.org/10.1002/9781119986928.ch3

Müntener, O., Hermann, J., 2001. The role of lower crust and continental upper mantle during formation of non-volcanic passive margins: evidence from the Alps. Geol. Soc. Lond. Spec. Publ. 187, 267–288. https://doi.org/10.1144/gsl.sp.2001.187.01.13

Müntener, O., Hermann, J., Trommsdorff, V., 2000. Cooling History and Exhumation of Lower-Crustal Granulite and Upper Mantle (Malenco, Eastern Central Alps). J. Petrol. 41, 175–200. https://doi.org/10.1093/petrology/41.2.175

Petri, B., Duretz, T., Mohn, G., Schmalholz, S.M., Karner, G.D., Müntener, O., 2019. Thinning mechanisms of heterogeneous continental lithosphere. Earth Planet. Sci. Lett. 512, 147–162. https://doi.org/10.1016/j.epsl.2019.02.007

Petri, B., Mohn, G., Skrzypek, E., Mateeva, Ts., Galster, F., Manatschal, G., 2017. U–Pb geochronology of the Sondalo gabbroic complex (Central Alps) and its position within the Permian post-Variscan extension. Int. J. Earth Sci. 106, 2873–2893. https://doi.org/10.1007/s00531-017-1465-x

Petri, B., Mohn, G., Štípská, P., Schulmann, K., Manatschal, G., 2016. The Sondalo gabbro contact aureole (Campo unit, Eastern Alps): implications for mid-crustal mafic magma emplacement. Contrib. Mineral. Petrol. 171, 52. https://doi.org/10.1007/s00410-016-1263-7

Petri, B., Skrzypek, E., Mohn, G., Mateeva, T., Robion, P., Schulmann, K., Manatschal, G., Müntener, O., 2018. Mechanical anisotropies and mechanisms of mafic magma ascent in the middle continental crust: The Sondalo magmatic system (N Italy). GSA Bull. 130, 331–352. https://doi.org/10.1130/B31693.1

Picazo, S.M., Ewing, T.A., Müntener, O., 2019. Paleocene metamorphism along the Pennine–Austroalpine suture constrained by U–Pb dating of titanite and rutile (Malenco, Alps). Swiss J. Geosci. 112, 517–542. https://doi.org/10.1007/s00015-019-00346-1

Platt, J.P., England, P.C., 1994. Convective removal of lithosphere beneath mountain belts; thermal and mechanical consequences. Am. J. Sci. 294, 307–336. https://doi.org/10.2475/ajs.294.3.307

Pohl, F., Froitzheim, N., Obermüller, G., Tomaschek, F., Schröder, O., Nagel, T.J., Sciunnach, D., Heuser, A., 2018. Kinematics and Age of Syn-Intrusive Detachment Faulting in the Southern Alps: Evidence for Early Permian Crustal Extension and Implications for the

Pangea A Versus B Controversy. Tectonics 37, 3668–3689. https://doi.org/10.1029/2018TC004974

Prijac, C., Doin, M.P., Gaulier, J.M., Guillocheau, F., 2000. Subsidence of the Paris Basin and its bearing on the late Variscan lithosphere evolution: a comparison between Plate and Chablis models. Tectonophysics 323, 1–38. https://doi.org/10.1016/S0040-1951(00)00100-1

Ribes, C., Ghienne, J.-F., Manatschal, G., Dall'Asta, N., Stockli, D.F., Galster, F., Gillard, M., Karner, G.D., 2020. The Grès Singuliers of the Mont Blanc region (France and Switzerland): stratigraphic response to rifting and crustal necking in the Alpine Tethys. Int. J. Earth Sci. 109, 2325–2352. https://doi.org/10.1007/s00531-020-01902-z

Schmidt, M.W., 1992. Amphibole composition in tonalite as a function of pressure: an experimental calibration of the Al-in-hornblende barometer. Contrib. Mineral. Petrol. 110, 304–310. https://doi.org/10.1007/BF00310745

Schuster, R., Stüwe, K., 2008. Permian metamorphic event in the Alps. Geology 36, 603–606. https://doi.org/10.1130/G24703A.1

Siegesmund, S., Layer, P., Dunkl, I., Vollbrecht, A., Steenken, A., Wemmer, K., Ahrendt, H., 2008. Exhumation and deformation history of the lower crustal section of the Valstrona di Omegna in the Ivrea Zone, southern Alps. Geol. Soc. Lond. Spec. Publ. 298, 45–68. https://doi.org/10.1144/sp298.3

Siivola, J., Schmid, R., 2007. List of Mineral abbreviations - Recommendations by the IUGS Subcomission on the Systematics of Metamorphic Rocks. IUGS Web Version 010207 1–14.

Smye, A.J., Stockli, D.F., 2014. Rutile U–Pb age depth profiling: A continuous record of lithospheric thermal evolution. Earth Planet. Sci. Lett. 408, 171–182. http://dx.doi.org/10.1016/j.epsl.2014.10.013

Sölva, H., Thöni, M., Habler, G., 2003. Dating a single garnet crystal with very high Sm/Nd ratios (Campo basement unit, Eastern Alps). Eur. J. Mineral. 15, 35–42. http://doi.org/10.1127/0935-1221/2003/0001-0035

Spillmann, P., Büchi, H.J., 1993. The Pre-Alpine Basement of the Lower Austro-Alpine Nappes in the Bernina Massif (Grisons, Switzerland; Valtellina, Italy), in: von Raumer, J.F., Neubauer, F. (Eds.), Pre-Mesozoic Geology in the Alps. Springer Berlin Heidelberg, pp. 457–467. https://doi.org/10.1007/978-3-642-84640-3_27

Stampfli, G.M., Kozur, H.W., 2006. Europe from the Variscan to the Alpine cycles. Geol. Soc. Lond. Mem. 32, 57–82. https://doi.org/doi:10.1144/gsl.mem.2006.032.01.04

Staudacher, T., Sarda, P., Richardson, S.H., Allègre, C.J., Sagna, I., Dmitriev, L. V, 1989. Noble gases in basalt glasses from a Mid-Atlantic Ridge topographic high at 14°N: geodynamic consequences. Earth Planet. Sci. Lett. 96, 119–133. http://dx.doi.org/10.1016/0012-821X(89)90127-1

Steiger, R.J., Jäger, E., 1977. Subcommission on geochronology: Convention on the use of decay constants in geo- and cosmochronology. Earth Planet. Sci. Lett. 36, 359–362. http://doi.org/10.1016/0012-821X(77)90060-7

Stein, C.A., Stein, S., 1992. A model for the global variation in oceanic depth and heat flow with lithospheric age. Nature 359, 123–129. https://doi.org/10.1038/359123a0

Tribuzio, R., Thirlwall, M.F., Messiga, B., 1999. Petrology, mineral and isotope geochemistry of the Sondalo gabbroic complex (Central Alps, Northern Italy): implications for the origin of

post-Variscan magmatism. Contrib. Mineral. Petrol. 136, 48–62. https://doi.org/10.1007/s004100050523

Vermeesch, P., 2018. IsoplotR: A free and open toolbox for geochronology. Geosci. Front. 9, 1479–1493. https://doi.org/10.1016/j.gsf.2018.04.001

Villa, I.M., Hermann, J., Müntener, O., Trommsdorff, V., 2000. 39Ar−40Ar dating of multiply zoned amphibole generations (Malenco, Italian Alps). Contrib. Mineral. Petrol. 140, 363–381. https://doi.org/10.1007/s004100000197

von Quadt, A., Grünenfelder, M., Büchi, H., 1994. U-Pb zircon ages from igneous rocks of the Bernina nappe system (Grisons, Switzerland). Schweiz. Mineral. Petrogr. Mitteilungen 74, 373–382.

Warren, C.J., Hanke, F., Kelley, S.P., 2012a. When can muscovite 40Ar/39Ar dating constrain the timing of metamorphic exhumation? Chem. Geol. 291, 79–86. https://doi.org/10.1016/j.chemgeo.2011.09.017

Warren, C.J., Kelley, S.P., Sherlock, S.C., McDonald, C.S., 2012b. Metamorphic rocks seek meaningful cooling rate: Interpreting 40Ar/39Ar ages in an exhumed ultra-high pressure terrane. Lithos 155, 30–48. https://doi.org/10.1016/j.lithos.2012.08.011

Wheeler, J., 1996. Diffarg: A program for simulating argon diffusion profiles in minerals. Comput. Geosci. 22, 919–929. http://dx.doi.org/10.1016/S0098-3004(96)00061-1

Wijbrans, J.R., Pringle, M.S., Koppers, A.A.P., Scheveers, R., 1995. Argon geochronology of small samples using the Vulkaan argon laserprobe. Proc. K. Ned. Akad. Van Weten Schappen - Biol. Chem. Geol. Phys. Med. Sci. 98, 185–218.

Wu, C.-M., Chen, H.-X., 2015. Calibration of a Ti-in-muscovite geothermometer for ilmenite- and Al2SiO5-bearing metapelites. Lithos 212–215, 122–127. https://doi.org/10.1016/j.lithos.2014.11.008